

Precise determination of α_s from the C -parameter distributionAndré H. Hoang,^{1,2} Daniel W. Kolodrubetz,³ Vicent Mateu,¹ and Iain W. Stewart³¹*University of Vienna, Faculty of Physics, Boltzmannngasse 5, A-1090 Wien, Austria*²*Erwin Schrödinger International Institute for Mathematical Physics, University of Vienna, Boltzmannngasse 9, A-1090 Vienna, Austria*³*Center for Theoretical Physics, Massachusetts Institute of Technology, Cambridge, Massachusetts 02139, USA*

(Received 20 January 2015; published 15 May 2015)

We present a global fit for $\alpha_s(m_Z)$, analyzing the available C -parameter data measured at center-of-mass energies between $Q = 35$ and 207 GeV. The experimental data is compared to a $N^3LL' + \mathcal{O}(\alpha_s^3) + \Omega_1$ theoretical prediction (up to the missing four-loop cusp anomalous dimension), which includes power corrections coming from a field-theoretical nonperturbative soft function. The dominant hadronic parameter is its first moment Ω_1 , which is defined in a scheme which eliminates the $\mathcal{O}(\Lambda_{\text{QCD}})$ renormalon ambiguity. The resummation region plays a dominant role in the C -parameter spectrum, and in this region a fit for $\alpha_s(m_Z)$ and Ω_1 is sufficient. We find $\alpha_s(m_Z) = 0.1123 \pm 0.0015$ and $\Omega_1 = 0.421 \pm 0.063$ GeV with $\chi^2/\text{d.o.f.} = 0.988$ for 404 bins of data. These results agree with the prediction of universality for Ω_1 between thrust and C -parameter within $1\text{-}\sigma$.

DOI: 10.1103/PhysRevD.91.094018

PACS numbers: 12.38.Bx, 12.38.-t, 12.38.Cy

I. INTRODUCTION

In order to study quantum chromodynamics (QCD) accurately in the high-energy regime, it is useful to exploit the wealth of data from previous e^+e^- colliders such as LEP. Here the final states coming from the underlying partons created in the collisions appear as boosted and collimated groups of hadrons known as jets. Event shapes have proven to be very successful to study these collisions quantitatively. They combine the energy and momenta of all of the measured hadrons into an infrared- and collinear-safe parameter which describes the geometric properties of the whole event by a single variable distribution. Due to their global nature event shapes have nice theoretical properties, making it possible to obtain very accurate theoretical predictions using QCD. Most e^+e^- event-shape variables quantify how well the event resembles the situation of two narrow back-to-back jets, called dijets, by vanishing in this limit. Because the dijet limit involves restrictions that only allow collinear and soft degrees of freedom for the final-state radiation, such QCD predictions involve a number of theoretical aspects that go beyond the calculation of higher-order perturbative loop corrections. These include factorization, to systematically account for perturbative and nonperturbative contributions, and the resummation of large logarithmic corrections by renormalization group evolution (RGE). Comparisons of predictions for event shapes with experimental data thus provide nontrivial tests of the dynamics of QCD.

Due to the high sensitivity of event shapes to jets induced by gluon radiation they are an excellent tool to measure the strong coupling α_s . For more inclusive hadronic cross sections (like $e^+e^- \rightarrow \text{hadrons}$) the α_s dependence is

subleading because it only occurs in corrections to a leading-order term, while for event shapes the α_s dependence is a leading-order effect. For this reason, the study of event shapes for determining α_s has a long history in the literature (see the review [1] and the workshop proceedings [2]), including recent analyses which include higher-order resummation and corrections up to $\mathcal{O}(\alpha_s^3)$ [3–12].

Several previous high-precision studies which determined $\alpha_s(m_Z)$ [4,5,9–11] focused on the event shape called thrust [13],

$$\tau = 1 - T = \min_{\vec{n}} \left(1 - \frac{\sum_i |\vec{n} \cdot \vec{p}_i|}{\sum_j |\vec{p}_j|} \right), \quad (1)$$

where \vec{n} is called the thrust axis and it follows from the above equation that $0 \leq \tau \leq 1/2$. Another event shape, known as C -parameter [14,15], can be written as

$$C = \frac{3}{2} \frac{\sum_{i,j} |\vec{p}_i| |\vec{p}_j| |\sin^2 \theta_{ij}|}{(\sum_i |\vec{p}_i|)^2}, \quad (2)$$

where θ_{ij} gives the angle between particles i and j . It is straightforward to show that $0 \leq C \leq 1$. In a previous paper [12] we computed the C -parameter distribution with a resummation of large logarithms at next-to-next-to-next-to-leading log prime (N^3LL') accuracy, including fixed-order terms up to $\mathcal{O}(\alpha_s^3)$ and hadronization effects using a field-theoretical nonperturbative soft function. These results were achieved by using the soft-collinear effective theory (SCET) [16–20]. Our results for C are valid in all three of the peak, tail, and far-tail regions of the distribution, and are the most accurate predictions available in the literature, having a perturbative uncertainty of $\approx 2.5\%$ at $Q = m_Z$ for

the region relevant for $\alpha_s(m_Z)$ and Ω_1 fits. The same accuracy was previously achieved for thrust, where the remaining perturbative uncertainty in the τ distribution is $\simeq 2\%$ in this region [9]. In this paper we make use of these new C -parameter theoretical results to carry out a global fit to all available data, comparing the results with the analogous global fit for thrust [9] where appropriate.

Since both τ and C vanish in the dijet limit, it is worthwhile to contrast them in order to anticipate differences that will appear in the analysis. Differences between C and τ include the following.

- (a) Calculating τ requires identifying the thrust axis with a minimization procedure, while C does not involve a minimization.
- (b) τ has a single sum over particles while C has a double sum.
- (c) The size of the nonperturbative region, where the entire shape function is important, is larger for C compared to τ due to an enhancement by a factor of $3\pi/2$.
- (d) The resummation region for C is larger than that for thrust since the logarithms appear as $\ln(C/6)$ compared to $\ln(\tau)$, which increases the range of C values that are useful for α_s fits.
- (e) Fixed-order predictions for the thrust cross section are smooth across the threshold where nonplanar events first contribute, $\tau = 1/3$, while the fixed-order C -parameter cross section has an integrable singularity at this threshold, $C_{\text{shoulder}} = 3/4$. The singularity for C comes from the fact that the leading-order distribution is not continuous at $C = C_{\text{shoulder}}$. (The C -distribution can be made smooth here using leading log resummation [21].)

A key similarity is that in the dijet limit ($C, \tau \ll 1$) the partonic cross sections for thrust and C -parameter are related up to next-to-leading log (NLL) by using $\tau = C/6$ [22]. This relation quantifies several qualitative relations between C and τ in the dijet region.

Recent higher-order event-shape analyses [4,9–11,11] have found values of $\alpha_s(m_Z)$ significantly lower than the world average of $\alpha_s(m_Z) = 0.1185 \pm 0.0006$ [23], which is dominated by the lattice QCD determination [24]. One result that gave a lower value was the determination carried out for thrust at $\text{N}^3\text{LL}' + \mathcal{O}(\alpha_s^3)$ in Ref. [9],¹ which is also consistent with analyses at $\text{N}^2\text{LL} + \mathcal{O}(\alpha_s^3)$ [11,25] which consider the resummation of logs at one lower order. In

¹Note that results at N^3LL require the currently unknown QCD four-loop cusp anomalous dimension, but conservative estimates show that this has a negligible impact on the perturbative uncertainties. Results at $\text{N}^3\text{LL}'$ also technically require the unknown three-loop nonlogarithmic constants for the jet and soft functions which are also varied when determining our uncertainties, but these parameters turn out to only impact the peak region which is outside the range of our $\alpha_s(m_Z)$ fits in the resummation region.

Ref. [26] a framework for a numerical code with N^2LL precision for many e^+e^- event shapes was found, which could also be utilized for α_s fits in the future. In Ref. [9] it was pointed out that including a proper fit to power corrections for thrust causes a significant negative shift to the value obtained for $\alpha_s(m_Z)$, and this was also confirmed by subsequent analyses [11]. Recent results for $\alpha_s(m_Z)$ from τ decays [27], deep inelastic scattering (DIS) data [28], the static potential for quarks [29], as well as global parton distribution function (PDF) fits [30,31] also find values below the world average. With the new analysis we present here, we provide another event-shape determination of $\alpha_s(m_Z)$ with a high level of precision. We will also simultaneously examine the leading power correction to the distribution, which should be universal between thrust and C -parameter.

This paper is organized as follows. In Sec. II we review the theoretical calculation of the C -parameter cross section, presented in more detail in Ref. [12]. The details on the experimental data and fit procedure used in our analysis are given in Secs. III and IV. In Sec. V we present the results of our fit for $\alpha_s(m_Z)$ and the first moment of the nonperturbative soft function, Ω_1 . Fits which include hadron-mass effects are discussed in Sec. V E. In Sec. VI we make predictions for the peak and far-tail regions of the distribution, which are not used in our fit, and compare those regions to experimental data. The universality of Ω_1 is discussed in Sec VII, where we compare our results with the previous fit done using thrust in Ref. [9]. Finally, Sec. VIII contains our conclusions. We also include three appendices. The first, Appendix A, contains the formulas needed to calculate the profile functions; the second, Appendix B, contains results that support our choice for the definition of the renormalon free Ω_1 parameter to use for C ; and the third compares fit results for thrust with our profiles and those from Ref. [9].

II. THEORY REVIEW

Until a few years ago, the theoretical uncertainties related to perturbative contributions as well as hadronic power corrections were still larger than the experimental uncertainties. The situation on the theory side has dramatically changed with the calculation of $\mathcal{O}(\alpha_s^3)$ corrections [3,7,32–35], and the pioneering use of SCET to obtain higher-order perturbative corrections in Ref. [5], and to obtain accurate predictions for the full spectrum and a precision description of power corrections in Ref. [9]. In this section we review the theoretical work behind our calculation of $d\sigma/dC$, presented in Ref. [12].

SCET separates the physics occurring at the different energy and momentum scales relevant to the underlying jets whose properties are characterized by an event shape. For the C -parameter distribution the relevant scales are: (i) the hard scale μ_H , which is related to the production of partons at short distances and is of the order of the

center-of-mass energy Q ; (ii) the jet scale $\mu_J \sim Q\sqrt{C}/6$, which governs the formation and evolution of the jets; and (iii) the soft scale $\mu_S \sim QC/6$, which is the scale of large-angle soft radiation. All three scales are widely separated in the dijet region $C \ll 1$, where most of the events occur and where the distribution is maximal. There is one function associated to each one of these scales in the factorization theorem that describes the dominant contribution of the C -parameter distribution in the dijet limit: (i) the hard function H (the modulus squared of the QCD-to-SCET matching coefficient), which is common to all dijet event-shape factorization theorems; (ii) the jet function J_τ (given by matrix elements of quark fields with collinear Wilson lines), which is common for C -parameter [12], thrust [9] and heavy jet mass (ρ) [8]; and (iii) the soft function $S_{\tilde{C}}$ (defined by a vacuum matrix element of purely soft Wilson lines), which in general depends on the specific form of the event shape. Whereas the former two are perturbative ($\mu_H, \mu_J \gg \Lambda_{\text{QCD}}$), permitting the calculation of the hard and jet functions as an expansion in powers of α_s , the soft function has perturbative corrections ($\mu_S \gg \Lambda_{\text{QCD}}$) as well as nonperturbative contributions that need to be accounted for ($\mu_S \gtrsim \Lambda_{\text{QCD}}$). Renormalization evolution between the three scales μ_H, μ_J , and μ_S sums up large logarithms to all orders in perturbation theory. It turns out that the soft function anomalous dimension for C and τ are identical [12], providing a connection between these two event shapes at every order of perturbation theory. Only corrections related to nonlogarithmic terms in their soft functions, and the associated towers of logarithms, differ between C and τ .

The soft function can be further factorized into a partonic soft function $\hat{S}_{\tilde{C}}$, calculable in perturbation theory, and a nonperturbative shape function F_C , which has to be obtained from fits to data. In the strict modified minimal subtraction ($\overline{\text{MS}}$) scheme this factorization was achieved in Refs. [36,37]. (Analytic power corrections for the C -parameter distributions have also been studied in other schemes and frameworks; see e.g. Refs. [38–40].)

The treatment of hadronic power corrections greatly simplifies in the tail of the distribution, defined by $QC \gg 3\pi\Lambda_{\text{QCD}}$, where the shape function can be expanded in an operator product expansion (OPE). Here the leading power correction is parametrized by Ω_1^C , the first moment of the shape function. The main effect of this leading power correction is a shift of the cross section, $d\hat{\sigma}(C) \rightarrow d\hat{\sigma}(C - \Omega_1^C/Q)$. Interestingly, this matrix element is related to the corresponding one in thrust by

$$\frac{\Omega_1^\tau}{2} = \frac{\Omega_1^C}{3\pi} \equiv \Omega_1. \quad (3)$$

This relation was first derived using dispersive models with a single soft-gluon approximation in Ref. [40]. The equality can actually be derived to all orders in QCD just using

quantum field theory [41], but ignoring hadron-mass effects [42]. These hadron-mass effects can also be formulated purely with quantum field theory operators [43]. Although they may in general give large corrections, hadron-mass effects turn out to violate Eq. (3) at only the 2% level, which is well below the 15% level determination of Ω_1 that we will achieve here. When presenting the results of our fits, we parametrize the power correction using Ω_1 defined in Eq. (3) to ease comparison with our previous analysis which determined this Ω_1 based on thrust [9,10].

A. Factorized cross section formula

In order to understand the perturbative components of the C -parameter cross section we make use of the C -parameter factorization formula. To make the connection to thrust simpler we will often use functions defined with the variable $\tilde{C} = C/6$. For the perturbative cross section we find [12]

$$\frac{1}{\sigma_0} \frac{d\hat{\sigma}_s}{dC} = \frac{Q}{6} H(Q, \mu) \int ds J_\tau(s, \mu) S_{\tilde{C}}\left(\frac{QC}{6} - \frac{s}{Q}, \mu\right). \quad (4)$$

Here J_τ is the thrust jet function, obtained by the convolution of the two hemisphere jet functions, $J_\tau = J \otimes J$. J_τ describes the collinear radiation in the direction of the two jets. Its definition and expression up to $\mathcal{O}(\alpha_s^3)$ [44–46] can be found in Refs. [5,9]. The three-loop nonlogarithmic coefficient of this jet function, j_3 , is not known, and we vary it in our scans. The anomalous dimension of J_τ is known at three loops, and can be obtained from Ref. [47].

The hard factor H contains short-distance QCD effects and is obtained from the Wilson coefficient of the QCD-SCET matching of the vector and axial-vector currents. The hard function is the same for all event shapes for massless quarks, and its expression up to $\mathcal{O}(\alpha_s^3)$ [48–52,52–54], can be found in Ref. [9]. The full anomalous dimension of H is known at three loops, $\mathcal{O}(\alpha_s^3)$ [49,51,55].

The soft function $S_{\tilde{C}}$ describes wide-angle soft radiation between the two jets. It is defined as

$$S_{\tilde{C}}(\ell, \mu) = \frac{1}{N_C} \langle 0 | \text{tr} \bar{Y}_n^T Y_n \delta\left(\ell - \frac{Q\hat{C}}{6}\right) Y_n^\dagger \bar{Y}_n^* | 0 \rangle, \quad (5)$$

where \hat{C} is an operator whose eigenvalues on physical states correspond to the value of C -parameter for that state: $\hat{C}|X\rangle = C(X)|X\rangle$. Since the hard and jet functions are the same as for thrust, the anomalous dimension of the soft function has to coincide with the anomalous dimension of the thrust soft function. Hence one only needs to determine the nonlogarithmic terms of the C -parameter soft function. In Ref. [12] we computed it analytically at one loop, $s_{\tilde{C}}^1 = -\pi^2 C_F/6$, and used EVENT2 to numerically determine the two-loop nonlogarithmic coefficient $s_{\tilde{C}}^2$, with the result

$$s_2^{\tilde{C}} = -43.2 \pm 1.0. \quad (6)$$

The three-loop nonlogarithmic coefficient of the C -parameter soft function, $s_3^{\tilde{C}}$, is currently not known, and we estimate it with a Padé approximation, assigning a very conservative uncertainty. We vary this constant in our scan analysis. The precise definitions of j_3 and $s_2^{\tilde{C}}$ as well as $s_3^{\tilde{C}}$ can be found in Eqs. (A10) and (A12) of Ref. [12], respectively.

In Eq. (4) the hard, jet and soft functions are evaluated at a common scale μ . If fixed-order expressions are used for these functions, then there is no scale choice that simultaneously minimizes the logarithms for these three functions. One can instead renormalization-group evolve from μ to the respective scales $\mu_H \sim Q$, $\mu_J \sim Q\sqrt{C/6}$ and $\mu_S \sim QC/6$ at which the logs in each of H , J_τ , and $S_{\tilde{C}}$ are minimized, and only use fixed-order expressions for these functions at these scales. In this way, large logs of ratios of the scales are summed up in the renormalization group evolution kernels U_H , U_J^τ , and U_S^τ :

$$\begin{aligned} \frac{1}{\sigma_0} \frac{d\hat{\sigma}_s}{dC} &= \frac{Q}{6} H(Q, \mu_H) U_H(Q, \mu_H, \mu) \\ &\times \int ds ds' J_\tau(s, \mu_J) U_J^\tau(s - s', \mu, \mu_J) \\ &\times \int dk U_S^\tau(k, \mu, \mu_S) S_{\tilde{C}}\left(\frac{QC}{6} - \frac{s}{Q} - k, \mu_S\right). \end{aligned} \quad (7)$$

The evolution kernels U_H , U_J^τ and U_S^τ resum the large logarithms, $\ln(C/6)$, and explicit expressions can be found in Ref. [12]. The only unknown piece in our resummation of logarithms at N³LL order is the small contribution from the four-loop cusp anomalous dimension, Γ_3^{cusp} , which we estimate using a Padé approximation and conservatively vary in our analysis.

While Eq. (7) gives the part of the cross section that is singular and nonintegrable as $C \rightarrow 0$, we also need to include the integrable or nonsingular contribution. This can be written as

$$\begin{aligned} \frac{1}{\sigma_0} \frac{d\hat{\sigma}_{\text{ns}}}{dC} &= \frac{\alpha_s(\mu_{\text{ns}})}{2\pi} f_1(C) \\ &+ \left(\frac{\alpha_s(\mu_{\text{ns}})}{2\pi}\right)^2 \left[f_2(C) + \beta_0 \ln\left(\frac{\mu_{\text{ns}}}{Q}\right) f_1(C) \right] \\ &+ \left(\frac{\alpha_s(\mu_{\text{ns}})}{2\pi}\right)^3 \left\{ f_3(C) + 2\beta_0 \ln\left(\frac{\mu_{\text{ns}}}{Q}\right) f_2(C) \right. \\ &+ \left. \left[\frac{\beta_1}{2} \ln\left(\frac{\mu_{\text{ns}}}{Q}\right) + \beta_0^2 \ln^2\left(\frac{\mu_{\text{ns}}}{Q}\right) \right] f_1(C) \right\} \\ &+ \mathcal{O}(\alpha_s^4). \end{aligned} \quad (8)$$

The functions $f_1(C)$, $f_2(C)$, and $f_3(C)$ were determined in Ref. [12] using the fixed-order results at $\mathcal{O}(\alpha_s^{1,2,3})$

[3,7,32–35,56–59]. The nonsingular cross section $d\hat{\sigma}_{\text{ns}}/dC$ is independent of the renormalization scale μ order by order, and therefore we evaluate these pieces at the nonsingular scale μ_{ns} , and vary this scale to estimate higher-order perturbative nonsingular corrections. The scale variation of μ_{ns} will be discussed further in Sec. II B.

The full partonic cross section is then given by

$$\frac{1}{\sigma_0} \frac{d\hat{\sigma}}{dC} = \frac{1}{\sigma_0} \frac{d\hat{\sigma}_s}{dC} + \frac{1}{\sigma_0} \frac{d\hat{\sigma}_{\text{ns}}}{dC}. \quad (9)$$

Nonperturbative effects are included by convolving Eq. (9) with a shape function:

$$\frac{1}{\sigma_0} \frac{d\sigma}{dC} = \int dp \frac{1}{\sigma_0} \frac{d\hat{\sigma}}{dC} \left(C - \frac{p}{Q} \right) F_C(p). \quad (10)$$

One important property of this shape function is that its first moment encodes the leading power correction to our cross section. In the $\overline{\text{MS}}$ scheme this moment is given by

$$\overline{\Omega}_1^C \equiv \int dk k F_C(k). \quad (11)$$

Up to the normalization factors shown in Eq. (3) we expect approximate universality between the Ω_1 for C -parameter and thrust. For the calculation of the cross section, the shape function is expanded in a complete basis of functions obtained by an appropriate infinite-range mapping of the Legendre polynomials [37], with the coefficients chosen to maintain the first moment. For further details on the implementation of the shape function for C -parameter see Ref. [12]. We remove an $\mathcal{O}(\Lambda_{\text{QCD}})$ renormalon by using the Rgap scheme [60,61], which introduces a subtraction scale R into our formula, as well as the gap parameter $\overline{\Delta}$ and the perturbative scheme-change gap parameter $\delta(R, \mu_S)$. Here, $\delta(R, \mu_S)$ is given by a perturbative series in $\alpha_s(\mu_S)$ whose mass dimension is set by an overall factor of R , and which also contains $\ln(\mu_S/R)$ factors. The convolution with the shape function now becomes,

$$\begin{aligned} \frac{d\sigma}{dC} &= \int dp e^{-3\pi \frac{\delta(R, \mu_S)}{Q} \frac{\partial}{\partial C}} \frac{d\hat{\sigma}}{dC} \left(C - \frac{p}{Q} \right) \\ &\times F_C(p - 3\pi \overline{\Delta}(R, \mu_S)). \end{aligned} \quad (12)$$

The final component of our cross section is properly accounting for hadron-mass effects following Ref. [43]. Hadron-mass effects induce an additional series of large perturbative logarithms which start at NLL, $\alpha_s^k \ln^k(\mu_S/\Lambda_{\text{QCD}})$, and also break the exact universality between Ω_1^C and Ω_1^τ given in Eq. (3). These effects are accounted for by including dependence on the transverse velocity, $r \equiv \frac{p_\perp}{\sqrt{p_\perp^2 + m_H^2}}$, in the nonperturbative matrix elements (here, m_H gives the nonzero hadron mass). In

particular, in the Rgap scheme the first moment of the shape function is actually given by

$$\begin{aligned} \int dk k F_C(k - 3\pi\bar{\Delta}(R, \mu_S)) &= \Omega_1^C(R, \mu_S) \\ &= 3\pi \int_0^1 dr g_C(r) \Omega_1(R, \mu_S, r). \end{aligned} \quad (13)$$

In the $\overline{\text{MS}}$ scheme the definition accounting for hadron-mass effects is the same as Eq. (13), but one sets $\bar{\Delta} = 0$ and removes R as an argument for these parameters. Accounting for both the $\overline{\text{MS}}$ running due to hadron masses and the R-evolution running in the Rgap scheme, the evolution of the integrand on the right-hand side of Eq. (13) is given by,

$$\begin{aligned} g_C(r) \Omega_1(R, \mu, r) &= g_C(r) \left[\frac{\alpha_s(\mu)}{\alpha_s(\mu_\Delta)} \right]^{\hat{\gamma}_1(r)} \Omega_1(R_\Delta, \mu_\Delta, r) \\ &+ \Delta^{\text{diff}}(R_\Delta, R, \mu_\Delta, \mu, r), \end{aligned} \quad (14)$$

where R_Δ and μ_Δ give the initial scales where the function $\Omega_1(R_\Delta, \mu_\Delta, r)$ is defined. The perturbative evolution kernel Δ^{diff} gives the R and μ running for each value of r . The function g_C encodes the event-shape dependence of the hadron-mass effects and $\hat{\gamma}_1$ gives the solution to the one-loop RGE for Ω_1 with hadron masses derived in Ref. [43]. Since the two- and three-loop r -dependent anomalous dimensions are unknown, we do not treat the logs generated by hadron-mass effects to the same level of precision. When hadron-mass effects are accounted for we always sum the associated logarithms at NLL. An analogous formula to Eq. (14) also holds for the thrust parameter Ω_1^r .

Combining all of these elements gives the complete cross section. Note that we can resum to any order up to $\text{N}^3\text{LL}'$ and can choose to include or leave out the shape function, renormalon subtraction and hadron-mass effects. This flexibility allows us to see how the analysis changes when we take into account each of these additional physical considerations and enables us to test how robust the fits are to various changes in the theoretical treatment.

B. Profile functions

In order to smoothly transition between the nonperturbative, resummation, and fixed-order regions we make use of profile functions $\mu_i(C)$ for the renormalization scales μ_H , $\mu_J(C)$, $\mu_S(C)$, $R(C)$, and $\mu_{\text{ns}}(C)$. In the three C regions, the requirements on the scales which properly deal with large logarithms, nonperturbative effects, and the cancellations between singular and nonsingular contributions in the fixed-order region are

- 1) nonperturbative: $C \lesssim 3\pi\Lambda_{\text{QCD}}$
 $\mu_H \sim Q, \quad \mu_J \sim \sqrt{\Lambda_{\text{QCD}} Q}, \quad \mu_S \sim R \sim \Lambda_{\text{QCD}},$
- 2) resummation: $3\pi\Lambda_{\text{QCD}} \ll C < 0.75$
 $\mu_H \sim Q, \quad \mu_J \sim Q\sqrt{\frac{C}{6}}, \quad \mu_S \sim R \sim \frac{QC}{6} \gg \Lambda_{\text{QCD}},$
- 3) fixed order: $C > 0.75$
 $\mu_{\text{ns}} = \mu_H = \mu_J = \mu_S = R \sim Q \gg \Lambda_{\text{QCD}}.$ (15)

In addition we take the fixed-order nonsingular scale $\mu_{\text{ns}} \sim \mu_H$ in the nonperturbative and resummation regions. Our profile functions $\mu_i(C)$ satisfy these constraints, and provide continuous and smooth transitions between these C regions. The resummed perturbative cross section is independent of $\mathcal{O}(1)$ variations in all renormalization scales order by order in the logarithmic resummation. Therefore the dependence on parameters appearing in the profile functions gets systematically smaller as we go to higher orders, and their variation provides us with a method of assessing perturbative uncertainties.

For the hard renormalization scale we use the C -independent formula

$$\mu_H = e_H Q, \quad (16)$$

where e_H is a parameter that we vary from 0.5 to 2 in order to account for theory uncertainties.

The soft scale has different functional dependence in the three regions of Eq. (15), and hence depends on the following parameters:

$$\mu_S = \mu_S(C, \mu_0, r_s, \mu_H, t_0, t_1, t_2, t_s). \quad (17)$$

Here, μ_0 controls the intercept of the soft scale at $C = 0$, t_0 is near the boundary of the purely nonperturbative region and t_1 controls the end of this transition, where the resummation region begins. The transition from nonperturbative to perturbative is Q dependent, so we use the Q -independent parameters $n_0 \equiv t_0 Q / (1 \text{ GeV})$ and $n_1 \equiv t_1 Q / (1 \text{ GeV})$. In the resummation region the parameter r_s determines the slope of the soft scale relative to the canonical resummation region scaling, with $\mu_S = r_s \mu_H C / 6$. The parameter t_2 controls where the transition occurs between the resummation and fixed-order regions and t_s sets the value of C where the renormalization scales all become equal as required in the fixed-order region. For the jet scale we have the dependence

$$\mu_J = \mu_J(\mu_H, \mu_S(C), e_J), \quad (18)$$

where e_J is a parameter that is varied in our theory scans to slightly modify the natural relation between the scales. The exact functional form for μ_S and μ_J in Eqs. (17) and (18) is given in Appendix A.

To avoid large logarithms in the soft function subtractions δ , the scale $R(C)$ is chosen to be the same as $\mu_S(C)$ in the resummation and fixed-order regions. In the nonperturbative region we need $R(C) < \mu_S(C)$ to obtain an $\mathcal{O}(\alpha_s)$ subtraction that stabilizes the soft function in this region (removing unphysical negative dips that appear in the $\overline{\text{MS}}$ scheme). This introduces an additional parameter $R_0 \equiv R(C=0)$. Therefore we have

$$R = R(\mu_S(C), R_0). \quad (19)$$

The exact functional form for R is also given in Appendix A.

For the nonsingular scale μ_{ns} , we use the variations

$$\mu_{\text{ns}}(C) = \begin{cases} \frac{1}{2}[\mu_H(C) + \mu_J(C)], & n_s = 1, \\ \mu_H, & n_s = 0, \\ \frac{1}{2}[3\mu_H(C) - \mu_J(C)], & n_s = -1. \end{cases} \quad (20)$$

Here the three choices vary μ_{ns} in a manner that allows it to have some independence from μ_H in the resummation and nonperturbative regions, while still being equal μ_H in the fixed-order region (where $\mu_J = \mu_H$). These variations of μ_{ns} probe the higher-order fixed-order uncertainty in the nonsingular cross section contribution. In the fixed-order region the variation of μ_H alone precisely reproduces the standard fixed-order scale variation.

The details of the variations of the profile function parameters used to assess uncertainties are given in Table I. The plot in Fig. 1 shows how the scales vary with the changes to our C -parameter profile parameters. The vertical arrow on the hard scale indicates the overall up/down variation, which causes a variation to all the scales. Also shown (as gray dashed lines) are plots of the canonical soft scale $QC/6$ and canonical jet scale $Q\sqrt{C}/6$. In the resummation region, these correspond fairly well with the profile functions, indicating that in this region our analysis will avoid large logarithms. As discussed in detail in Ref. [12], to improve the convergence of the C -parameter cross sections we take $r_s = 2$ as our default slope parameter, explaining why our soft and jet scales are larger than the canonical values in Fig. 1 (by a factor that does not induce further large logs). In the analysis of Sec. V, we will see how varying each of these profile parameters affects our final fit results.

For the numerical analyses carried out in this work we have created within our collaboration two completely independent codes. One code within MATHEMATICA [62] implements the theoretical expressions exactly as given in Ref. [12], and another code is based on theoretical formulas in Fourier space and realized as a fast FORTRAN [63] code suitable for parallelized runs on computer clusters. These two codes agree for the C -parameter distribution at the level of 10^{-6} .

TABLE I. C -parameter theory parameters relevant for estimating the theory uncertainty, their default values and range of values used for the theory scan during the fit procedure. The last four parameters control the statistical errors induced by fit functions used in the nonsingular terms at $\mathcal{O}(\alpha_s^2)$ (ϵ_2^{low} and ϵ_2^{high}) and $\mathcal{O}(\alpha_s^3)$ (ϵ_3^{low} and ϵ_3^{high}) in the region below (ϵ_2^{low} and ϵ_3^{low}) and above (ϵ_2^{high} and ϵ_3^{high}) the shoulder; see Sec. V of Ref. [12].

Parameter	Default value	Range of values
μ_0	1.1 GeV	...
R_0	0.7 GeV	...
n_0	12	10 to 16
n_1	25	22 to 28
t_2	0.67	0.64 to 0.7
t_s	0.83	0.8 to 0.86
r_s	2	1.78 to 2.26
e_J	0	-0.5 to 0.5
e_H	1	0.5 to 2.0
n_s	0	-1, 0, 1
Γ_3^{cusp}	1553.06	-1553.06 to +4659.18
\tilde{S}_2^{C}	-43.2	-44.2 to -42.2
j_3	0	-3000 to +3000
\tilde{S}_3^{C}	0	-500 to +500
ϵ_2^{low}	0	-1, 0, 1
ϵ_2^{high}	0	-1, 0, 1
ϵ_3^{low}	0	-1, 0, 1
ϵ_3^{high}	0	-1, 0, 1

We will also repeat the thrust fits of Ref. [9], implementing the same type of profile functions used here. These profiles have several advantages over those in Ref. [9], including a free variable for the slope, a flat nonperturbative region, and parameters whose impact is much more confined to one of the three regions in Eq. (15). For the thrust profiles we redefine $r_s \rightarrow 6r_s$, which eliminates the factors of 6 in Eqs. (A1) and (A4). This way, the canonical

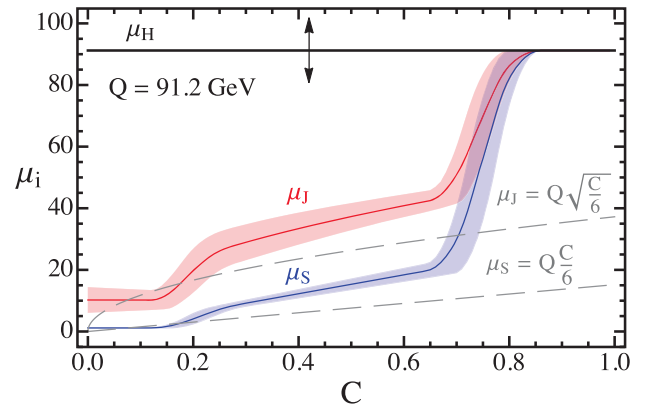


FIG. 1 (color online). Bands for the profile functions for the renormalization scales μ_H , $\mu_J(C)$, $\mu_S(C)$ when varying the profile parameters.

TABLE II. Thrust theory parameters relevant for estimating the theory uncertainty, their default values and range of values used for the theory scan during the fit procedure. The last two parameters control the statistical errors induced by fit functions used in the nonsingular terms at $\mathcal{O}(\alpha_s^2)$ (ϵ_2) and $\mathcal{O}(\alpha_s^3)$ (ϵ_3); see Sec. E of Ref. [9].

Parameter	Default value	Range of values
μ_0	1.1 GeV	...
R_0	0.7 GeV	...
n_0	2	1.5 to 2.5
n_1	10	8.5 to 11.5
t_2	0.25	0.225 to 0.275
t_s	0.4	0.375 to 0.425
r_s	2	1.77 to 2.26
e_J	0	-1.5 to 1.5
e_H	1	0.5 to 2.0
n_s	0	-1, 0, 1
j_3	0	-3000 to +3000
s_3^τ	0	-500 to +500
ϵ_2	0	-1, 0, 1
ϵ_3	0	-1, 0, 1

choice of slope is $r_s = 1$ for both C -parameter and thrust. We use $r_s = 2$ as our default for thrust as well, again to improve the perturbative convergence, as discussed in Ref. [12]. The profile parameters for thrust and their variations are summarized in Table II. These choices create profiles that are very similar to those used in Ref. [9]. The new fit results for thrust are fully compatible with those of Ref. [9] in the resummation region used for the α_s fits. Additionally, they give a better description in the non-perturbative region which is outside of our fit range.

C. Hadron-mass effects

In Ref. [43] it was shown that hadron-mass effects, apart from breaking the universality properties of the leading power correction for various event shapes, also induce a nontrivial running. Since these are single logarithms, they start at NLL order. In Ref. [43] the corresponding leading anomalous dimension was determined, which yields the NLL resummation of larger logs between the scales μ_S and Λ_{QCD} for a large set of event shapes. The pieces necessary for a higher-order resummation have not yet been computed. One might be worried that accounting for only the NLL running for Ω_1 in an expression as accurate as N³LL in cross-section logs could be inadequate, or that it could leave significant perturbative uncertainties. However, one should recall that the hadronic parameter Ω_1 itself is a correction, and hence it is valid to account for the related resummation with less precision. In this section we show that the Ω_1 evolution at NLL order suffices for the precision of our N³LL' + $\mathcal{O}(\alpha_s^3)$ analysis. Indeed, it turns out that the effect of the hadron-mass running on the fit outcome is very small as compared to other uncertainties, and therefore can be safely neglected.

For our C -parameter analysis the implementation of hadron-mass running effects has been explained at length in Ref. [12], and we only summarize here the most relevant aspects needed to understand the fit results. In the $\overline{\text{MS}}$ scheme the leading power correction can be written as an integral of a universal hadron function, $\overline{\Omega}_1(\mu, r)$, common to all event shapes

$$\overline{\Omega}_1^e(\mu) = c_e \int_0^1 dr g_e(r) \overline{\Omega}_1(\mu, r), \quad (21)$$

where r is the transverse velocity, e denotes a specific event shape, c_e is a calculable normalization factor, and $g_e(r)$ is an event-shape-dependent function encoding the hadron-mass effects. The functions $g_e(r)$ are known analytically, and specific examples can be found in Ref. [43]. For C -parameter $c_C = 3\pi$, while for thrust $c_\tau = 2$. For the simple case of the $\overline{\text{MS}}$ scheme the running between the initial reference scale μ_0 where the universal hadron function is specified, and the soft scale μ_S , is given at leading order by

$$\overline{\Omega}_1(\mu_S, r) = \overline{\Omega}_1(\mu_0, r) \left[\frac{\alpha_s(\mu_S)}{\alpha_s(\mu_0)} \right]^{\hat{\gamma}_1(r)}, \quad (22)$$

with $\hat{\gamma}_1(r) = \frac{2C_A}{\beta_0} \ln(1-r^2)$. The corresponding evolution formula for the Rgap scheme is considerably more complex, as shown by the form displayed in Eq. (14) above. Ensuring that the renormalon is not reintroduced by the renormalization group evolution requires an additional evolution in the scale R , so $\Delta^{\text{diff}}(R_\Delta, R, \mu_\Delta, \mu, r)$ contains evolution in both the μ and R scales. Also here we have two reference scales μ_Δ and R_Δ to specify the initial parameter $\Omega_1(R_\Delta, \mu_\Delta, r)$. The full formula for Δ^{diff} is given in Eq. (67) of Ref. [12].

Note that the renormalization group evolution is a function of r and takes place independently for each r , but the required result for C -parameter or thrust requires an integral over r . Due to this integration the functional form that we assume for the initial condition $\overline{\Omega}_1(r, \mu_0)$ or $\Omega_1(R_\Delta, \mu_\Delta, r)$ gets entangled with the perturbative resummation.

With current constraints on the r dependence, and with the lack of even more precise experimental data to probe this issue, a model-independent formulation (like a complete functional basis for the r dependence at the reference scales, R_Δ and μ_Δ) is not feasible. To implement this running we have therefore tested several models for the r dependence in Ref. [12], and found that generically the experimental data is sensitive to the normalization which specifies Ω_1 , but not to the detailed form used for the r dependence as long as it satisfies several reasonable constraints. Therefore for the fits performed here we simply adopt the default form from Ref. [12],

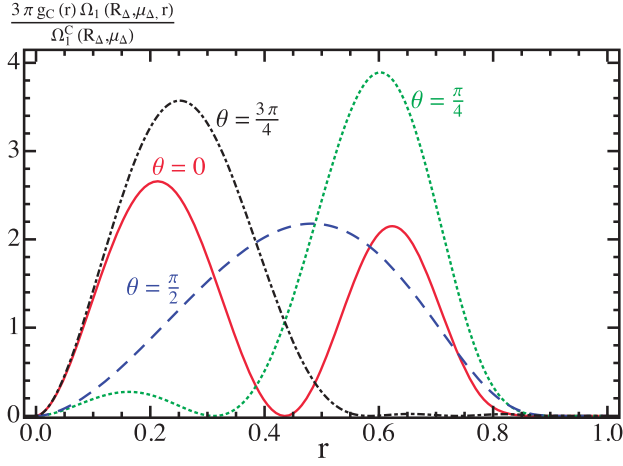


FIG. 2 (color online). Plots of the r dependence of $g_C(r)\Omega_1(R_\Delta, \mu_\Delta, r)$ for different values of $\theta(R_\Delta, \mu_\Delta)$. We normalize to $\Omega_1^C(R_\Delta, \mu_\Delta)$, since it is simply an overall multiplicative factor.

$$\begin{aligned} \Omega_1(R_\Delta, \mu_\Delta, r) &= [a(R_\Delta, \mu_\Delta)f_a(r) + b(R_\Delta, \mu_\Delta)f_b(r)]^2, \\ f_a(r) &= 3.510e^{-\frac{r^2}{1-r^2}}, \\ f_b(r) &= 13.585e^{-\frac{2r^2}{1-r^2}} - 21.687e^{-\frac{4r^2}{1-r^2}}. \end{aligned} \quad (23)$$

This model ensures that $\Omega_1(R_\Delta, \mu_\Delta, r)$ is always positive definite and smoothly goes to zero at the $r = 1$ endpoint (where the ratio of the hadron mass to p_T goes to zero). The functions $f_{a,b}$ form an orthonormal basis upon integration with $g_C(r)$, which yields the following relation:

$$\Omega_1^C(R_\Delta, \mu_\Delta) = 3\pi[a(R_\Delta, \mu_\Delta)^2 + b(R_\Delta, \mu_\Delta)^2], \quad (24)$$

which determines the normalization. We also define

$$\theta(R_\Delta, \mu_\Delta) \equiv \arctan\left(\frac{b(R_\Delta, \mu_\Delta)}{a(R_\Delta, \mu_\Delta)}\right), \quad (25)$$

which was chosen to have an effect orthogonal to the more relevant parameter $\Omega_1^C(R_\Delta, \mu_\Delta)$. By examining our ability to simultaneously measure $\Omega_1^C(R_\Delta, \mu_\Delta)$ and $\theta(R_\Delta, \mu_\Delta)$ we have a means to test for the impact that the initial r dependence has on our fits. As we can see in Fig. 2, our model captures different behavior for the r dependence of $\Omega_1(R_\Delta, \mu_\Delta, r)$ by choosing different values of $\theta(R_\Delta, \mu_\Delta)$. Over the interval $r \in [0, 1]$, all the curves in this figure are normalized so that they integrate to 1.

III. EXPERIMENTAL DATA

Data on the C -parameter cross section are given by several experiments for a range of Q from 35 to 207 GeV. We use data from ALEPH² with $Q = \{91.2, 133, 161, 172, 183, 189, 200, 206\}$ GeV [64], DELPHI with $Q = \{45, 66,$

76, 89.5, 91.2, 93, 133, 161, 172, 183, 189, 192, 196, 200, 202, 205, 207\} GeV [65–68], JADE with $Q = \{35, 44\}$ GeV [69], L3 with $Q = \{91.2, 130.1, 136.1, 161.3, 172.3, 182.8, 188.6, 194.4, 200.2, 206.2\}$ GeV [70,71], OPAL with $Q = \{91, 133, 177, 197\}$ GeV [72], and SLD with $Q = 91.2$ GeV [73]. As each of these data sets is given in binned form, our cross section in Eq. (12) is integrated over each bin before being compared to the data. The default range on C used in fitting the data is $25 \text{ GeV}/Q \leq C \leq 0.7$. A lower limit of $25 \text{ GeV}/Q$ eliminates the peak region where higher nonperturbative moments $\Omega_{n>1}^C$ become important. The upper limit is chosen to be 0.7 in order to avoid the far-tail region as well as the Sudakov shoulder at $C = 0.75$. Any bin that contains one of the endpoints of our range ($C = 25 \text{ GeV}/Q$ or 0.7) is included if more than half of that bin lies within the range. Using the default range and data sets gives a total of 404 bins. As a further test of the stability of our analysis, both this C -parameter range and the selection of data sets is varied in the numerical analysis contained in Sec. V.

In our fitting procedure, we consider both the statistical and systematic experimental uncertainties. The statistical uncertainties can be treated as independent between bins. The systematic experimental uncertainties come from various sources and full documentation of their correlations are not available, so dealing with them in our χ^2 analysis is more complicated, and we have to use a correlation model. For this purpose we follow the LEP QCD Working Group [64,72] and use the minimal overlap model. Within one C -parameter data set, which consists of various C -parameter bins at one Q value for one experiment, we take for the bin i , bin j off-diagonal entry of the experimental covariance matrix $[\min(\Delta_i^{\text{sys}}, \Delta_j^{\text{sys}})]^2$. Here $\Delta_{i,j}^{\text{sys}}$ are the quoted systematic uncertainties of the bins i and j . Within each data set, this model implies a positive correlation of systematic uncertainties. In addition to this default model choice, we also do the fits assuming uncorrelated systematic uncertainties, in order to test whether the minimal overlap model introduces any bias. See Sec. VB for more details on the correlation matrix.

IV. FIT PROCEDURE

In order to accurately determine both $\alpha_s(m_Z)$ and the leading power correction in the same fit, it is important to perform a global analysis, that is, simultaneously fitting C -spectra for a wide range of center-of-mass energies Q . For each Q , effects on the cross sections induced by changes in $\alpha_s(m_Z)$ can be partly compensated by changes in Ω_1 , resulting in a fairly strong degeneracy. This is resolved by

²The ALEPH data set with $Q = 91.2$ GeV has two systematic uncertainties for each bin. The second of these uncertainties is treated as correlated while the first one is treated as an uncorrelated uncertainty and simply added in quadrature to the statistical uncertainty.

the global fit, just as in the thrust analysis of Ref. [9]. Figure 3 shows the difference between the theoretical prediction for the cross section at three different values of Q , when $\alpha_s(m_Z)$ or Ω_1 are varied by ± 0.001 and ± 0.05 GeV, respectively. It is clear that the potential degeneracy in these parameters is broken by having data at multiple Q values. In Fig. 3 we also vary the higher-order power correction parameter Ω_2^C , which

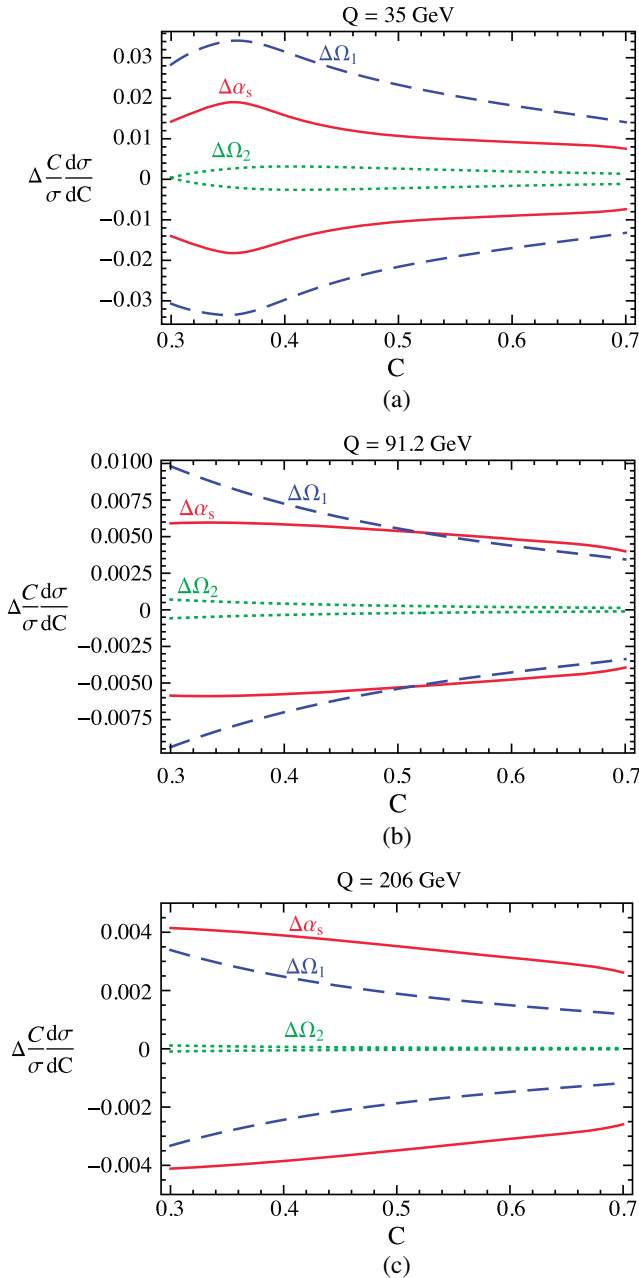


FIG. 3 (color online). Difference between the default cross section and the cross section varying only one parameter. We vary $\alpha_s(m_Z)$ by ± 0.001 (solid red), $2\Omega_1$ by ± 0.1 (dashed blue) and Ω_2^C by ± 0.5 (dotted green). The three plots correspond to three different center-of-mass energies: (a) $Q = 35$ GeV, (b) $Q = 91.2$ GeV, (c) $Q = 206$ GeV.

clearly has a much smaller effect than the dominant power correction parameter Ω_1 .

To carry out a fit to the experimental data we fix the profile and theory parameters to the values shown in Table I. The default values are used for our primary theory cross section. We integrate the resulting theoretical distribution over the same C -parameter bins as those available experimentally, and construct a χ^2 function with the uncorrelated statistical experimental uncertainties and correlated systematic uncertainties. This χ^2 is a function of $\alpha_s(m_Z)$ and Ω_1 , and is very accurately described by a quadratic near its global minimum, which therefore determines the central values and experimental uncertainties. The value of Ω_1 and its associated uncertainties encode the dominant hadronization effect as well as the dominant residual uncertainty from hadronization.

To obtain the perturbative theoretical uncertainty we consider the range of values shown for the theory parameters in Table I. Treating each of these as a flat distribution, we randomly generate values for each of these parameters and then repeat the fit described above with the new χ^2 function. This random sampling and fit is then repeated 500 times. We then construct the minimum ellipse that fully contains all 500 of the central-fit values by first creating the convex envelope that contains all of these points within it. Then, we find the equation for the ellipse that best fits the points on the envelope, with the additional restrictions that all values lie within the ellipse and its center is the average of the maximum and minimum values in each direction. This ellipse determines the perturbative theoretical uncertainty, which turns out to be the dominant uncertainty in our fit results. In our final results the perturbative and experimental uncertainties are added in quadrature. This procedure is similar to that discussed in the Appendix of Ref. [10].

V. RESULTS

In this section we discuss the results from our global analysis. We split the presentation into several subsections. In Sec. VA we discuss the impact that resummation and the inclusion of power corrections have on the fit results. In Sec. VB we present the analysis which yields the perturbative uncertainty in detail, cross-checking our method by analyzing the order-by-order convergence. We also analyze the impact of removing the renormalon. In Sec. VC we discuss the experimental uncertainties obtained from the fit. Section VD discusses the impact that varying the theory parameters one by one has on the best-fit points, allowing us to determine which parameters dominate the theoretical uncertainty. The impact of hadron-mass resummation is discussed in detail in Sec. VE. We examine the effects of changing the default data set in Sec. VF. The final fit results are collected in Sec. VG. When indicating the perturbative precision, and whether or not the power correction Ω_1 is included and at what level of precision, we use the following notation:

$\mathcal{O}(\alpha_s^k)$	fixed order up to $\mathcal{O}(\alpha_s^k)$,
$N^kLL' + \mathcal{O}(\alpha_s^k)$	perturbative resummation,
$N^kLL' + \mathcal{O}(\alpha_s^k) + \overline{\Omega}_1$	\overline{MS} scheme for Ω_1 ,
$N^kLL' + \mathcal{O}(\alpha_s^k) + \Omega_1(R, \mu)$	Rgap scheme for Ω_1 ,
$N^kLL' + \mathcal{O}(\alpha_s^k) + \Omega_1(R, \mu, r)$	Rgap scheme with hadron masses for Ω_1 .

A. Impact of resummation and power corrections

In Fig. 4 we show $\alpha_s(m_Z)$ extracted from fits to the tail of the C -parameter distribution including sequential improvements to the treatment of perturbative and nonperturbative components of our code, using the highest perturbative accuracy at each stage. The sequence from left to right shows the fit results using $\mathcal{O}(\alpha_s^3)$ fixed-order results only, adding N^3LL resummation, adding the $\overline{\Omega}_1$ power correction, adding renormalon subtractions and using the Rgap power correction parameter $\Omega_1(R_\Delta, \mu_\Delta)$, and adding hadron-mass effects. These same results together with the corresponding $\chi^2/\text{d.o.f.}$ are also collected in Table III. The fit with only fixed-order $\mathcal{O}(\alpha_s^3)$ results has a relatively large $\chi^2/\text{d.o.f.}$ and also its central value has the largest value of $\alpha_s(m_Z)$. Including the resummation of large logarithms decreases the central $\alpha_s(m_Z)$ by 8% and also decreases the perturbative uncertainty by $\sim 50\%$. Due to this smaller perturbative uncertainty it becomes clear that the theoretical cross section has a different slope than the data, which can be seen, for example, at $Q = m_Z$ for $0.27 < C < 0.35$. This leads to the increase in the $\chi^2/\text{d.o.f.}$ for the “ N^3LL' no power corr.” fit, and makes it quite obvious that power corrections are needed. When the power correction parameter Ω_1 is included in the fit, shown by the

TABLE III. Comparison of C -parameter tail fit results for analyses when we add various components of the theoretical result (from the bottom to top). The first parentheses gives the theory uncertainty, and the second is the experimental and hadronic uncertainties added in quadrature for the first three rows, and experimental uncertainty for the last two rows.

	$\alpha_s(m_Z)$	$\chi^2/\text{d.o.f.}$
$N^3LL' + \text{hadron}$	0.1119(13)(06)	0.991
N^3LL' with $\Omega_1(R, \mu)$	0.1123(14)(06)	0.988
N^3LL' with $\overline{\Omega}_1$	0.1117(16)(06)	1.004
N^3LL' no power corr.	0.1219(28)(02)	2.091
$\mathcal{O}(\alpha_s^3)$ fixed order no power corr.	0.1317(52)(03)	1.486

third entry in Table III and the result just to the right of the vertical dashed line in Fig. 4, the $\chi^2/\text{d.o.f.}$ becomes 1.004 and this issue is resolved. Furthermore, a reduction by $\sim 50\%$ is achieved for the perturbative uncertainty in $\alpha_s(m_Z)$. This reduction makes sense since some of the perturbative uncertainty of the cross section is now absorbed in Ω_1 , and a much better fit is achieved for any of the variations associated to estimating higher-order corrections. The addition of Ω_1 also caused the fit value of $\alpha_s(m_Z)$ to drop by another 8%, consistent with our expectations for the impact of power corrections and the estimate made in Ref. [12]. Note that the error bars of the first two purely perturbative determinations, shown on the left-hand side of the vertical thick dashed line in Fig. 4 and in the last two entries in Table III, do not include the $\sim 8\%$ uncertainties associated with the lack of power corrections.

The remaining corrections we consider are the use of the R -scheme for Ω_1 which includes the renormalon subtractions,

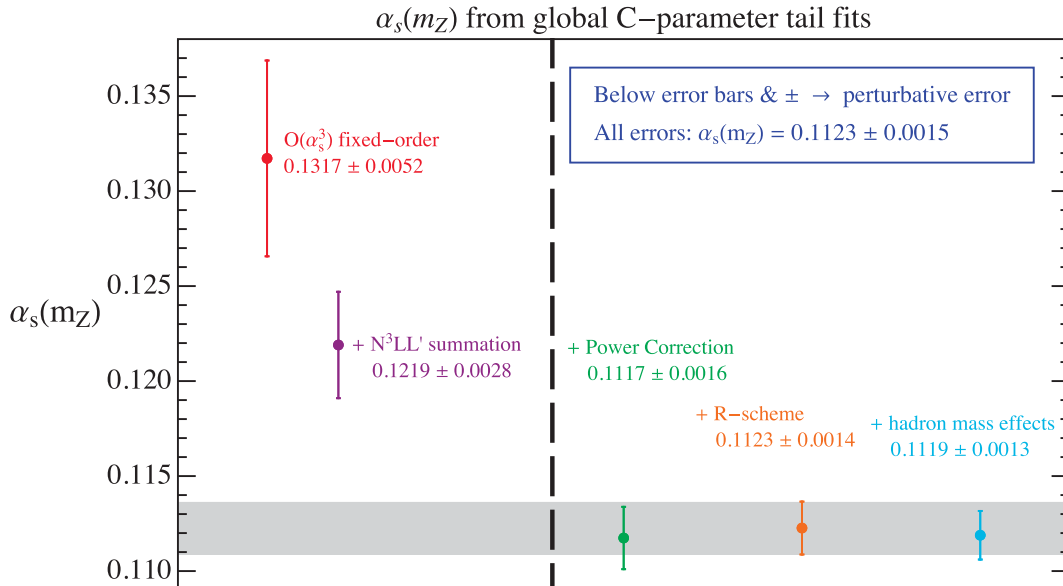


FIG. 4 (color online). The evolution of the value of $\alpha_s(m_Z)$ adding components of the calculation. An additional $\sim 8\%$ uncertainty from not including power corrections is not included in the two left points.

and the inclusion of the log-resummation effects associated to the hadron-mass effects. Both of these corrections have a fairly small impact on the determination of $\alpha_s(m_Z)$, shifting the central value by $+0.5\%$ and -0.3% respectively. Since adding the -0.3% shift from the hadron-mass corrections in quadrature with the $\approx 1.2\%$ perturbative uncertainty does not change the overall uncertainty we will use the R-scheme determination for our main result. This avoids the need to fully

discuss the extra fit parameter $\theta(R_\Delta, \mu_\Delta)$ that appears when hadron masses are included. Further discussion of the experimental uncertainties and the perturbative uncertainty from the random scan are given below in Secs. VB and VD, and a more detailed discussion of the impact of hadron-mass resummation is given below in Sec. VE.

The values of Ω_1 obtained from the fits discussed above can be directly compared to the Ω_1 power correction

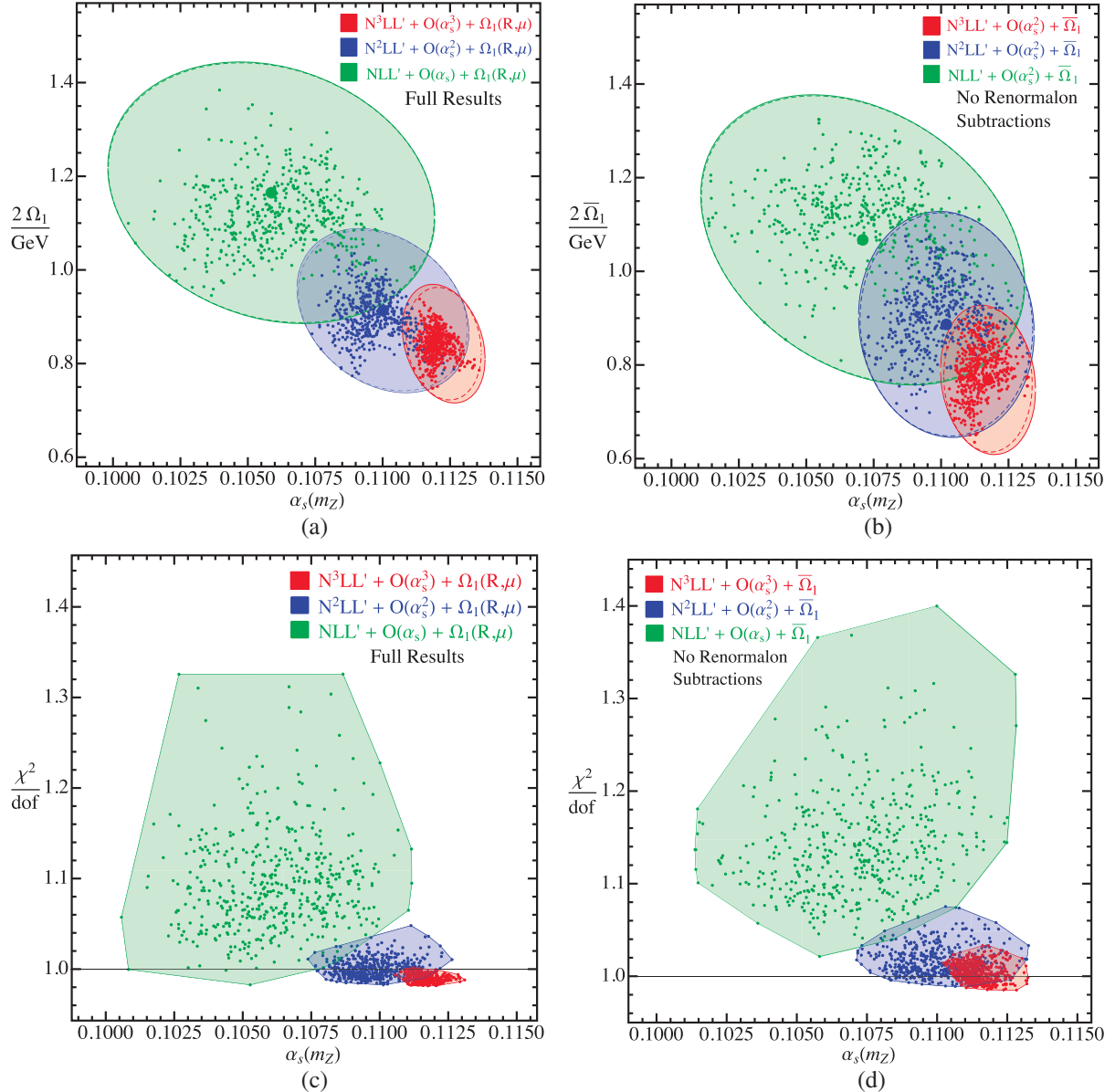


FIG. 5 (color online). The first two panels show the distribution of best-fit points in the $\alpha_s(m_Z)$ - $2\Omega_1$ and $\alpha_s(m_Z)$ - $2\bar{\Omega}_1$ planes. Panel (a) shows results including perturbation theory, resummation of large logs, the soft nonperturbative function and Ω_1 defined in the Rgap scheme with renormalon subtractions. Panel (b) shows the results as in panel (a), but with $\bar{\Omega}_1$ defined in the $\overline{\text{MS}}$ scheme without renormalon subtractions. In both panels the dashed lines corresponds to an ellipse fit to the contour of the best-fit points to determine the theoretical uncertainty. The respective total (experimental + theoretical) 39% C.L. standard uncertainty ellipses are displayed (solid lines), which correspond to 1- σ (68% C.L.) for either one-dimensional projection. The big points represent the central values in the random scan for $\alpha_s(m_Z)$ and $2\Omega_1$. Likewise, the two panels at the bottom show the distribution of best-fit points in the $\alpha_s(m_Z)$ - $\chi^2/\text{d.o.f.}$ plane. Panel (c) shows the $\chi^2/\text{d.o.f.}$ values of the points given in panel (a), whereas panel (b) shows the $\chi^2/\text{d.o.f.}$ values of the points given in panel (b).

obtained from the thrust distribution. Values for Ω_1 from the C -parameter fits are given below in Secs. VB and VD and the comparison with thrust is considered in Sec. VII.

B. Perturbative uncertainty from the scan

To examine the robustness of our method of determining the perturbative uncertainty by the random scan, we consider the convergence and overlap of the results at different perturbative orders. Figure 5 shows the spread of best-fit values at NLL', N²LL' and N³LL'. The upper left panel, Fig. 5(a), shows results from fits performed in the Rgap scheme, which implements a renormalon subtraction for Ω_1 , and the upper right panel, Fig. 5(b), shows results in the $\overline{\text{MS}}$ scheme without renormalon subtractions. Each point in the plot represents the outcome of a single fit, and different colors correspond to different orders in perturbation theory. Not unexpectedly, fits in the Rgap scheme show generally smaller theory uncertainties.

In order to estimate correlations induced by theoretical uncertainties, each ellipse in the α_s - $2\Omega_1$ plane is constructed following the procedure discussed in Sec. IV. Each theory ellipse constructed in this manner is interpreted as an estimate for the $1\text{-}\sigma$ theoretical uncertainty ellipse for each individual parameter (39% confidence for the two parameters), and is represented by a dashed ellipse in Fig. 5. The solid lines represent the combined (theoretical plus experimental) standard uncertainty ellipses at 39% confidence for two parameters, obtained by adding the theoretical and experimental error matrices from the individual ellipses, where the experimental ellipse corresponds to $\Delta\chi^2 = 1$. Figure 5 clearly shows a substantial reduction of the perturbative uncertainties when increasing the resummation accuracy, and given that they are 39% confidence regions for two parameters, also show good overlap between the results at different orders.

The results for $\alpha_s(m_Z)$ and Ω_1 from the theory scan at different perturbative orders are collected in Tables IV and V. Central values here are determined from the average of the maximal and minimal values of the theory scan, and are very close to the central values obtained when running with our default parameters. The quoted perturbative uncertainties are one-parameter uncertainties.

In Table III above we also present $\alpha_s(m_Z)$ results with no power corrections and either using resummation

TABLE IV. Central values for $\alpha_s(m_Z)$ at various orders with theory uncertainties from the parameter scan (first value in parentheses), and experimental and hadronic uncertainty added in quadrature (second value in parentheses). The bold N³LL' value is our final result.

Order	$\alpha_s(m_Z)$ (with $\overline{\Omega}_1$)	$\alpha_s(m_Z)$ [with $\Omega_1(R_\Delta, \mu_\Delta)$]
NLL'	0.1071(60)(05)	0.1059(62)(05)
N ² LL'	0.1102(32)(06)	0.1100(33)(06)
N ³ LL' (full)	0.1117(16)(06)	0.1123(14)(06)

TABLE V. Central values for Ω_1 at the reference scales $R_\Delta = \mu_\Delta = 2$ GeV and for $\overline{\Omega}_1$ and at various orders. The parentheses show first the theory uncertainties from the parameter scan, and second the experimental plus the uncertainty due to the imprecise determination of α_s (added in quadrature). The bold N³LL' value is our final result.

Order	$\overline{\Omega}_1$ [GeV]	$\Omega_1(R_\Delta, \mu_\Delta)$ [GeV]
NLL'	0.533(154)(18)	0.582(134)(16)
N ² LL'	0.443(119)(19)	0.457(83)(19)
N ³ LL' (full)	0.384(91)(20)	0.421(60)(20)

or fixed-order perturbative results. Without power corrections there is no fit for Ω_1 , so we take the central value to be the average of the maximum and minimum value of $\alpha_s(m_Z)$ that comes from our parameter scan. Our estimate of the uncertainty is given by the difference between our result and the maximum fit value. For the fixed-order case, since there is only one renormalization scale, we know that the uncertainties from our parameter variation for $e_H, s_2^{\overline{C}}, e_2^{\text{low}}$ and e_3^{low} are uncorrelated. So, we take the fit value for $\alpha_s(m_Z)$ with the default parameters as our result and add the uncertainties from variations of these parameter in quadrature to give the total uncertainty.

An additional attractive result of our fits is that the experimental data is better described when increasing the order of the resummation and fixed-order terms. This can be seen by looking at the minimal $\chi^2/\text{d.o.f.}$ values for the best-fit points, which are shown in Fig. 5. In Figs. 5(c) and 5(d) we show the distribution of $\chi_{\text{min}}^2/\text{d.o.f.}$ values for the various $\alpha_s(m_Z)$ best-fit points. Figure 5(c) displays the results in the Rgap scheme, whereas Fig. 5(d) shows the results in the $\overline{\text{MS}}$ scheme. In both cases we find that the χ_{min}^2 values systematically decrease with increasing perturbative order. The highest-order analysis in the $\overline{\text{MS}}$ scheme leads to $\chi_{\text{min}}^2/\text{d.o.f.}$ values around unity and thus provides an adequate description of the whole data set; however, one also observes that accounting for the renormalon subtraction in the Rgap scheme leads to a substantially improved theoretical description having $\chi_{\text{min}}^2/\text{d.o.f.}$ values below unity essentially for all points in the random scan. Computing the average of the χ_{min}^2 values we find at N³LL' order for the Rgap and $\overline{\text{MS}}$ schemes 0.988 and 1.004, respectively (where the spread of values is smaller in the Rgap scheme). Likewise for N²LL' we find 1.00 and 1.02, and for NLL' we find 1.09 and 1.14. These results show the excellent description of the experimental data for various center-of-mass energies. They also validate the smaller theoretical uncertainties obtained for α_s and Ω_1 at N²LL' and N³LL' orders in the Rgap scheme.

C. Experimental fit uncertainty

Next we discuss in more detail the experimental uncertainty in $\alpha_s(m_Z)$ and the hadronization parameter Ω_1 as

well as the combination with the perturbative uncertainty done to obtain the total uncertainty.

Results are depicted in Fig. 6 for our highest-order fit including resummation, power corrections and renormalon subtractions. The inner green dotted ellipse, blue dashed ellipse, and solid red ellipse represent the $\Delta\chi^2 = 1$ uncertainty ellipses for the experimental, theoretical, and combined theoretical and experimental uncertainties respectively. These ellipses correspond to the one-dimensional projection of the uncertainties onto either $\alpha_s(m_Z)$ or Ω_1 (39% confidence ellipse for two parameters). The correlation matrix of the experimental, theory, and total uncertainty ellipses are (for $i, j = \alpha_s, 2\Omega_1$),

$$V_{ij} = \begin{pmatrix} \sigma_{\alpha_s}^2 & 2\sigma_{\alpha_s}\sigma_{\Omega_1}\rho_{\alpha\Omega} \\ 2\sigma_{\alpha_s}\sigma_{\Omega_1}\rho_{\alpha\Omega} & 4\sigma_{\Omega_1}^2 \end{pmatrix},$$

$$V_{ij}^{\text{exp}} = \begin{pmatrix} 4.18(52) \cdot 10^{-7} & -0.24(5) \cdot 10^{-4} \text{ GeV} \\ -0.24(5) \cdot 10^{-4} \text{ GeV} & 1.60(47) \cdot 10^{-3} \text{ GeV}^2 \end{pmatrix},$$

$$V_{ij}^{\text{theo}} = \begin{pmatrix} 1.93 \cdot 10^{-6} & -0.27 \cdot 10^{-4} \text{ GeV} \\ -0.27 \cdot 10^{-4} \text{ GeV} & 1.45 \cdot 10^{-2} \text{ GeV}^2 \end{pmatrix},$$

$$V_{ij}^{\text{tot}} = \begin{pmatrix} 2.35(5) \cdot 10^{-6} & -0.51(5) \cdot 10^{-4} \text{ GeV} \\ -0.51(5) \cdot 10^{-4} \text{ GeV} & 1.61(5) \cdot 10^{-2} \text{ GeV}^2 \end{pmatrix}. \quad (26)$$

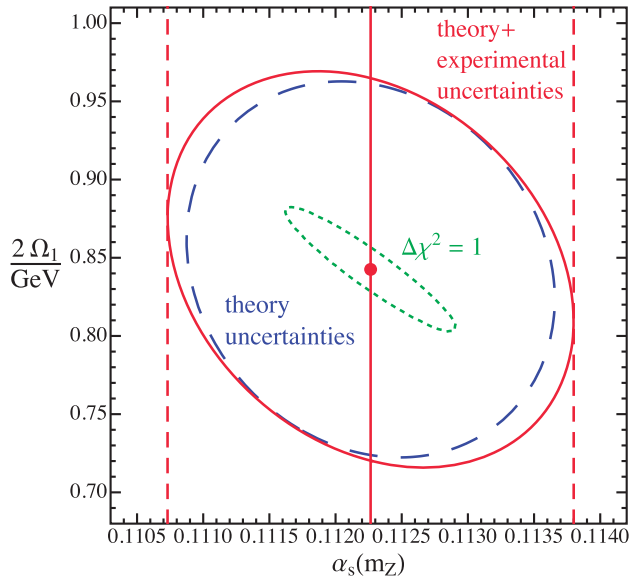


FIG. 6 (color online). Experimental $\Delta\chi^2 = 1$ standard uncertainty ellipse (dotted green) at $N^3\text{LL}'$ accuracy with renormalon subtractions, in the α_s - $2\Omega_1$ plane. The dashed blue ellipse represents the theory uncertainty which is obtained by fitting an ellipse to the contour of the distribution of the best-fit points. This ellipse should be interpreted as the $1\text{-}\sigma$ theory uncertainty for one parameter (39% confidence for two parameters). The solid red ellipse represents the total (combined experimental and perturbative) uncertainty ellipse.

Note that the theoretical uncertainties dominate by a significant amount. The experimental correlation coefficient is significant and reads

$$\rho_{\alpha\Omega}^{\text{exp}} = -0.93(15). \quad (27)$$

The theory correlation coefficient is small, $\rho_{\alpha\Omega}^{\text{theo}} = -0.16$, and since these uncertainties dominate it reduces the correlation coefficient for the total uncertainty to

$$\rho_{\alpha\Omega}^{\text{total}} = -0.26(2). \quad (28)$$

In both Eqs. (27) and (28) the numbers in parentheses indicate a \pm range that captures all values obtained from the theory scan. The correlation exhibited by the green dotted experimental uncertainty ellipse in Fig. 6 is given by the line describing the semimajor axis

$$\frac{\Omega_1}{30.84 \text{ GeV}} = 0.1257 - \alpha_s(m_Z). \quad (29)$$

Note that extrapolating this correlation to the extreme case where we neglect the nonperturbative corrections ($\Omega_1 = 0$) gives $\alpha_s(m_Z) \rightarrow 0.1257$ which is consistent with the 0.1219 ± 0.0028 result of our fit without power corrections in Table III.

From V_{ij}^{exp} in Eq. (26) it is possible to extract the experimental uncertainty for $\alpha_s(m_Z)$ and the uncertainty due to the imprecise determination of Ω_1 ,

$$\sigma_{\alpha_s}^{\text{exp}} = \sigma_{\alpha_s} \sqrt{1 - \rho_{\alpha\Omega}^2} = 0.0002,$$

$$\sigma_{\alpha_s}^{\Omega_1} = \sigma_{\alpha_s} |\rho_{\alpha\Omega}| = 0.0006, \quad (30)$$

and to extract the experimental uncertainty for Ω_1 and its uncertainty due to the imprecise determination of $\alpha_s(m_Z)$,

$$\sigma_{\Omega_1}^{\text{exp}} = \sigma_{\Omega_1} \sqrt{1 - \rho_{\alpha\Omega}^2} = 0.014 \text{ GeV},$$

$$\sigma_{\Omega_1}^{\alpha_s} = \sigma_{\Omega_1} |\rho_{\alpha\Omega}| = 0.037 \text{ GeV}. \quad (31)$$

The projections of the outer solid ellipse in Fig. 6 show the total uncertainty in our final one-parameter results obtained from V_{ij}^{tot} , which are quoted below in Eq. (34).

D. Individual theory scan errors

To gain further insight into our theoretical precision and in order to estimate the dominant source for theory uncertainty from missing higher-order terms, we look at the size of the theory uncertainties caused by the individual variation of each one of the theory parameters included in our random scan. In Fig. 7 two bar charts are shown with these results for $\alpha_s(m_Z)$ (left panel) and $\Omega_1(R_\Delta, \mu_\Delta)$ (right panel) for fits corresponding to our best theoretical setup (with $N^3\text{LL}'$ accuracy and in the Rgap scheme). The dark blue bars correspond to the result of the fit with an upward

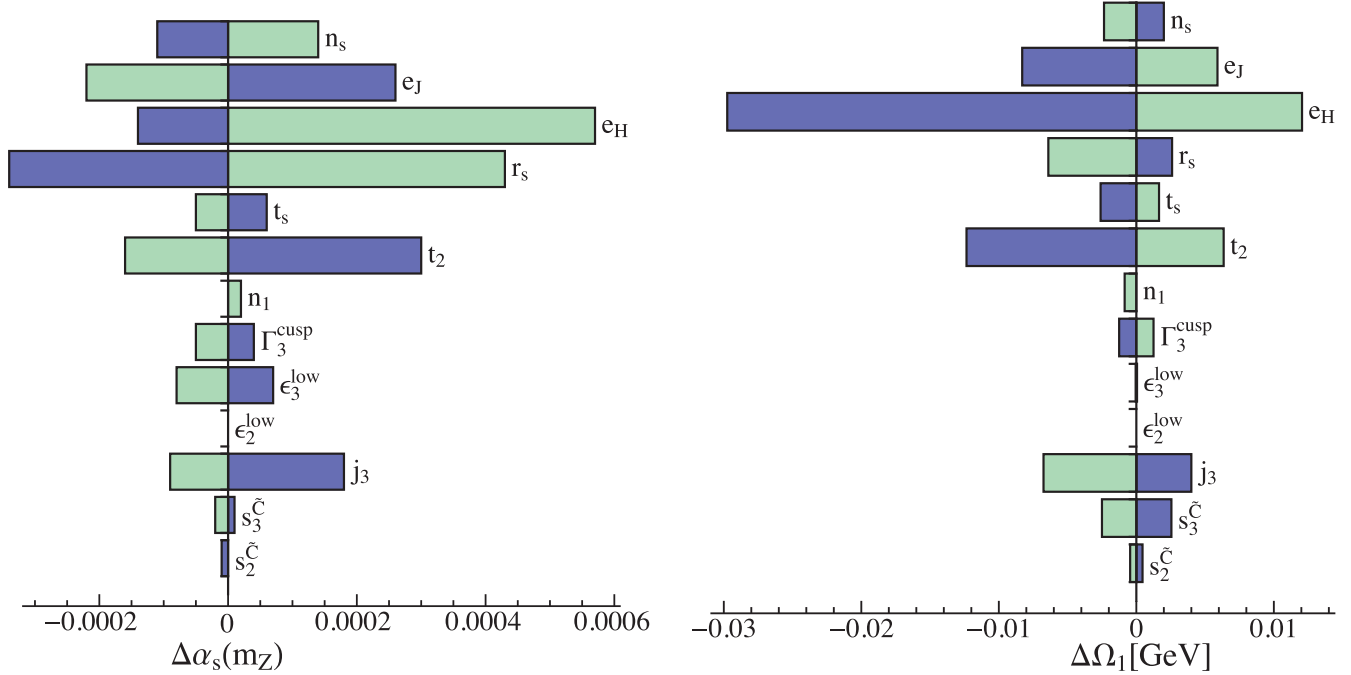


FIG. 7 (color online). Variations of the best-fit values for $\alpha_s(m_Z)$ and Ω_1 from up (dark blue) and down (light green) variations for the theory parameters according to Table I. We do not display those parameters which do not affect the fit region (ϵ_2^{high} , ϵ_3^{high} , μ_0 , R_0 , n_0).

variation of the given parameter from Table I, while the light green bars correspond to the fit result from the downward variation in Table I. Here we vary a single parameter keeping the rest fixed at their default values. We do not show parameters that have a negligibly small impact in the fit region, e.g. ϵ_2^{high} and ϵ_3^{high} , which only have an effect on the cross section to the right of the shoulder, or n_0 , which only affects the cross section in the nonperturbative region.

We see that the dominant theory uncertainties are related to variations of the profile functions (e_H , r_s , e_J , t_2), where e_H is the largest source of uncertainty, and is particularly dominant for Ω_1 . The second most important uncertainty comes from r_s for α_s and t_2 for Ω_1 , and e_J also has a significant effect on both parameters.

As expected, the parameters associated to the transitions on the sides of our fit region, n_1 and t_s , hardly matter. The renormalization scale parameter n_s for the nonsingular partonic distribution $d\hat{\sigma}_{\text{ns}}/dC$ also causes a very small uncertainty since the nonsingular terms are always dominated by the singular terms in our fit region. The uncertainties related to the numerical uncertainties of the perturbative constants ($s_2^{\tilde{C}}$, $s_3^{\tilde{C}}$, j_3) as well as the numerical uncertainties in the extraction of the nonsingular distribution for small C values, (ϵ_2^{low} , ϵ_3^{low}) are—with the possible exception of j_3 —much smaller and do not play an important role. The uncertainty related to the unknown four-loop contribution to the cusp anomalous dimension is always negligible. Adding quadratically the symmetrized individual uncertainties shown in Fig. 7, we find 0.0007 for

α_s and 0.05 GeV for Ω_1 . This is about one half of the theoretical uncertainty we have obtained by the theory parameter scan for α_s (or five sixths for Ω_1), demonstrating that incorporating correlated variations through the theory parameter scan represents a more realistic method to estimate the theory uncertainty.

E. Effects of Ω_1 hadron-mass resummation

The fit results presented in the previous two sections ignored the small hadron-mass effects. These effects are analyzed in greater detail in this section. We again perform 500 fits for a theory setup which includes $N^3\text{LL}'$ accuracy and a power correction in the Rgap scheme, but this time it also includes hadron-mass-induced running.

Since the impact of hadron-mass effects is small, one finds that the experimental data in the tail of the distribution is not accurate enough to fit for $\theta(R_\Delta, \mu_\Delta)$ in Eq. (25), in addition to $\alpha_s(m_Z)$ and $\Omega_1(R_\Delta, \mu_\Delta)$. This is especially true because it enters as a small modification to the power correction, which by itself is not the dominant term. Indeed, fitting for $a(R_\Delta, \mu_\Delta)$ and $b(R_\Delta, \mu_\Delta)$ as defined in Eq. (23) gives a strongly correlated determination of these two parameters. The dominant hadronic parameter $\Omega_1^C(R_\Delta, \mu_\Delta)$, which governs the normalization, is still as accurately determined from data as the Ω_1 in Table V. However, the orthogonal parameter $\theta(R_\Delta, \mu_\Delta)$ is only determined with very large statistical uncertainties. As discussed in Ref. [12], the specific value of $\theta(R_\Delta, \mu_\Delta)$ has a very small impact on the cross section, which is consistent with the inability to accurately fit for it.

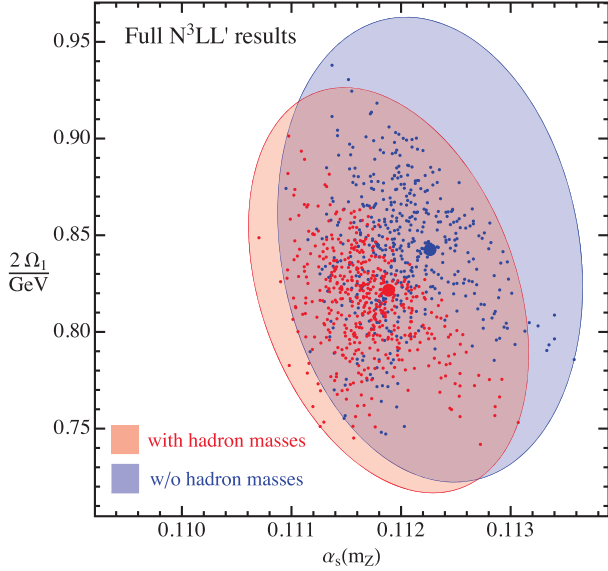


FIG. 8 (color online). Comparison of fits to the C -parameter tail distribution with theory prediction which include/ignore hadron-mass effects (in red/blue). Although a direct comparison of α_s values is possible, one has to keep in mind that $\Omega_1(\mu_\Delta, R_\Delta)$ has a different meaning once hadron-mass running effects are included.

The results of our fit including hadron-mass effects are

$$\alpha_s(m_Z) = 0.1119 \pm 0.0006_{\text{exp+had}} \pm 0.0013_{\text{pert}},$$

$$\Omega_1(R_\Delta, \mu_\Delta) = 0.411 \pm 0.018_{\text{exp}+\alpha_s} \pm 0.052_{\text{pert}} \text{ GeV}. \quad (32)$$

Note that the meaning of $\Omega_1(R_\Delta, \mu_\Delta)$ here is different from the case in which hadron-mass running effects are ignored because there are extra evolution effects needed to translate this value to that used in the cross section at a given value of C , compared to the no-hadron-mass case.

In Fig. 8 we compare the outcome of the 500 fits at N^3LL' in the Rgap scheme. Results with hadron-mass effects give the red ellipse on the left, and those without hadron-mass effects give the blue ellipse on the right. (The latter ellipse is the same as the one discussed above in Sec. V B.) The effects of hadron masses on $\alpha_s(m_Z)$ are to decrease its central value by 0.3% and reduce the percent perturbative uncertainty by 0.1%. Given that the total perturbative uncertainties are 1.2%, these effects are not statistically significant. When studying the effect on Ω_1 one has to keep in mind that its meaning changes when hadron-mass effects are included. Ignoring this fact we observe that hadron masses shift the central value downwards by 2.4%, and reduce the percent theoretical uncertainty by 1.6%. Again, given that the perturbative uncertainty for Ω_1 is 14%, this shift is not significant.

Since the theory uncertainties become slightly smaller when hadron-mass effects are incorporated, one could use this setup as our default. However we take a more conservative approach and consider the 0.3% shift on the central value as an additional source of uncertainty,

to be added in quadrature to the hadronization uncertainty already discussed in Sec. V B. This increases the value of the hadronization uncertainty from 0.0006 to 0.0007, and does not affect the total α_s uncertainty. The main reason we adopt this more conservative approach is that, while well motivated, the ansatz that we take in Eq. (23) is not model independent. We believe that this ansatz serves as a good estimate of what the numerical effect of hadron masses are, but should likely not be used for the central fit until further theoretical insight on the form of $\Omega_1(r)$ is gained. We do not add an additional uncertainty to Ω_1 since hadron-mass effects change its meaning and uncertainties for Ω_1 are large enough that these effects are negligible.

In Appendix B we also consider fits performed using the Rgap scheme with C -parameter gap subtractions, rather than our default Rgap scheme with thrust gap subtractions. The two results are fully compatible. As discussed in Ref. [12] the thrust gap subtractions give better perturbative convergence, and hence are used for our default cross section.

F. Data set dependence

In this section we discuss how much our results depend on the data set choice. Our default global data set accounts for all experimental bins for $Q \geq 35$ GeV in the intervals $[C_{\min}, C_{\max}] = [25/Q, 0.7]$ (more details are given in Sec. III). The upper limit in this range is motivated by the fact that we do not want to include data too close to the shoulder, since we do not anticipate having the optimal theoretical description of this region. The lower limit avoids including data too close to the nonperturbative region, which is near the cross section peak for $Q = m_Z$, since we by default only include the leading power correction Ω_1 in the OPE of the shape function. To consider the impact of this data set choice we can vary the upper and lower limits used to select the data.

In Fig. 9 the best fits and the respective total experimental + theory 68% C.L. uncertainty ellipses (for two parameters) are shown for global data sets based on different choices of data ranges. The result for our default global data set is given in red, with a thicker, dashed ellipse. In the caption of Fig. 9 the data ranges and the number of bins are specified for each one of the plotted ellipses.

Interestingly all uncertainty ellipses have very similar correlation and are lined up approximately along the line

$$\frac{\Omega_1}{41.26 \text{ GeV}} = 0.1221 - \alpha_s(m_Z). \quad (33)$$

As expected, the results of our fits depend only weakly on the C range and the size of the global data sets, as shown in Fig. 9. The size and tilt of the total uncertainty ellipses is very similar for all data sets (with the exception of $[22/Q, 0.7]$, which clearly includes too much peak data). Since the centers and the sizes of the uncertainty ellipses

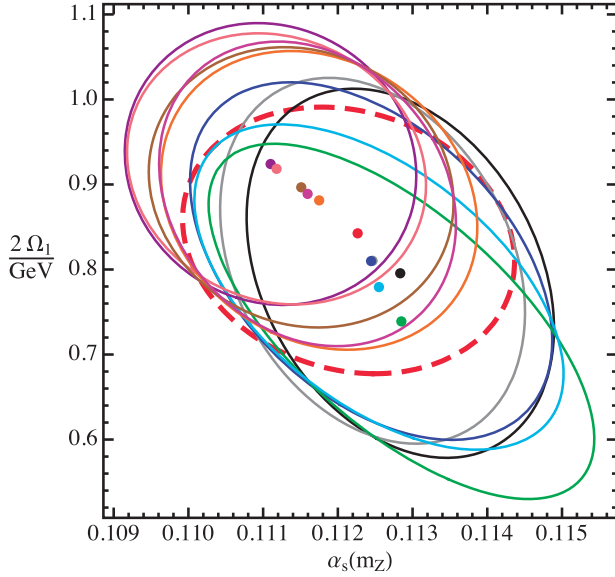


FIG. 9 (color online). Global fit results for different choices of data set, using our best theory setup at N^3LL' with power corrections in the Rgap scheme. Considering the central values from left to right, the data sets read $[C_{\min}, C_{\max}]_{\text{of bins}}$: $[29/Q, 0.7]_{371}$, $[22/Q, 0.75]_{453}$, $[23/Q, 0.7]_{417}$, $[0.24, 0.75]_{403}$, $[24/Q, 0.7]_{409}$, $[25/Q, 0.7]_{404}$ (default), $[25/Q, 0.6]_{322}$, $[25/Q, 0.75]_{430}$, $[27/Q, 0.7]_{386}$, $[25/Q, 0.65]_{349}$, $[22/Q, 0.7]_{427}$. We accept bins which are at least 50% inside these fit regions. The ellipses correspond to total $1\text{-}\sigma$ uncertainties (experimental + theory) for two variables (α_s and Ω_1), which are suitable for a direct comparison of the outcome of two-parameter fits. The center of the ellipses are also shown.

are fully statistically compatible at the $1\text{-}\sigma$ level, this indicates that our theory uncertainty estimate at N^3LL' really reflects the accuracy at which we are capable of describing the different regions of the spectrum. Therefore a possible additional uncertainty that one could consider due to the arbitrariness of the data set choice is actually already represented in our final uncertainty estimates.

G. Final results

As our final result for $\alpha_s(m_Z)$ and Ω_1 , obtained at N^3LL' order in the Rgap scheme for $\Omega_1(R_\Delta, \mu_\Delta)$, we get

$$\begin{aligned} \alpha_s(m_Z) &= 0.1123 \pm 0.0002_{\text{exp}} \\ &\quad \pm 0.0007_{\text{hadr}} \pm 0.0014_{\text{pert}}, \\ \Omega_1(R_\Delta, \mu_\Delta) &= 0.421 \pm 0.007_{\text{exp}} \\ &\quad \pm 0.019_{\alpha_s(m_Z)} \pm 0.060_{\text{pert}} \text{ GeV}, \end{aligned} \quad (34)$$

where $R_\Delta = \mu_\Delta = 2 \text{ GeV}$ and we quote individual $1\text{-}\sigma$ uncertainties for each parameter. Here $\chi^2/\text{d.o.f.} = 0.99$. Equation (34) is the main result of this work.

Equation (34) accounts for the effect of hadron-mass running through an additional (essentially negligible)

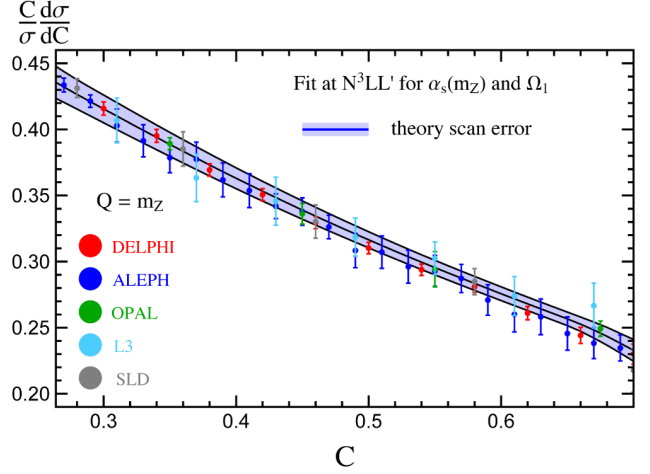


FIG. 10 (color online). C -parameter distribution at N^3LL' order for $Q = m_Z$ showing the fit result for the values for $\alpha_s(m_Z)$ and Ω_1 . The blue band corresponds to the theory uncertainty as described in Sec. V B. Experimental data is also shown.

uncertainty. Also, it neglects QED and finite bottom-mass corrections, which were found to be small effects in the corresponding thrust analysis of Ref. [9].

Given that we treat the correlation of the systematic experimental uncertainties in the minimal overlap model, it is useful to examine the results obtained when assuming that all systematic experimental uncertainties are uncorrelated. At N^3LL' order in the Rgap scheme the results that are analogous to Eq. (34) read $\alpha_s(m_Z) = 0.1123 \pm 0.0002_{\text{exp}} \pm 0.0007_{\text{hadr}} \pm 0.0012_{\text{pert}}$ and $\Omega_1(R_\Delta, \mu_\Delta) = 0.412 \pm 0.007_{\text{exp}} \pm 0.022_{\alpha_s} \pm 0.061_{\text{pert}} \text{ GeV}$ with a combined correlation coefficient of $\rho_{\alpha\Omega}^{\text{total}} = -0.091$. The results are compatible with Eq. (34), indicating that the ignorance of the precise correlation of the systematic experimental uncertainties barely affects the outcome of the fit.

In Fig. 10 we show the theoretical fit for the C -parameter distribution in the tail region, at a center-of-mass energy corresponding to the Z -pole. We use the best-fit values given in Eq. (34). The band corresponds to the perturbative uncertainty as determined by the scan. The fit result is shown in comparison with experimental data from DELPHI, ALEPH, OPAL, L3 and SLD. Good agreement is observed for this spectrum, as well as for spectra at other center-of-mass values.

VI. PEAK AND FAR-TAIL PREDICTIONS

Even though our fits were performed in the resummation region which is dominated by tail data, our theoretical results also apply for the peak and far-tail regions. As an additional validation for the results of our global analysis in the tail region, we use the best-fit values obtained for α_s and Ω_1 to make predictions in the peak and the far-tail regions where the corresponding data was not included in the fit.

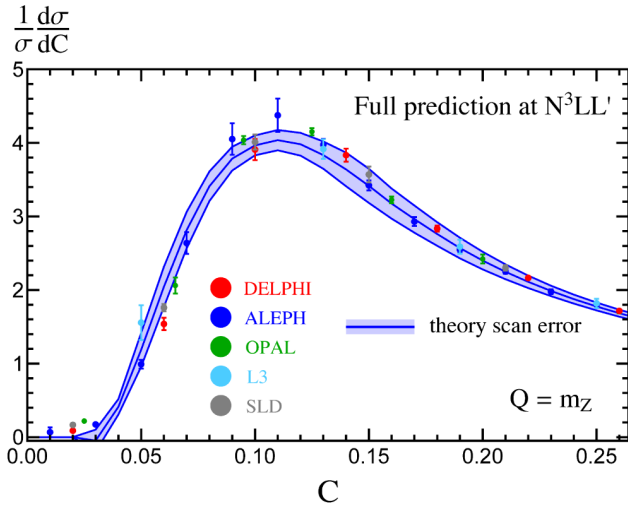


FIG. 11 (color online). C -parameter distribution below the fit region, shown at N^3LL' order for $Q = m_Z$ using the best-fit values for $\alpha_s(m_Z)$ and Ω_1 . Again the blue band corresponds to the theory uncertainty and error bars are used for experimental data.

Predictions from our full N^3LL' code in the Rgap scheme for the C -parameter cross section at the Z -pole in the peak region are shown in Fig. 11. The nice agreement within theoretical uncertainties (blue band) with the precise data from DELPHI, ALEPH, OPAL, L3, and SLD indicates that the value of Ω_1 obtained from the fit to the tail region is the dominant nonperturbative effect in the peak. The small deviations between the theory band and the experimental data can be explained due to the fact that the peak is also sensitive to higher-order power corrections $\Omega_{k \geq 2}^C$, which have not been tuned to reproduce the peak data in our analysis.

In Fig. 12 we compare predictions from our full N^3LL' code in the Rgap scheme to the accurate DELPHI, ALEPH, L3, and SLD data at $Q = m_Z$ in the far-tail region.³ We find excellent agreement with the data within the theoretical uncertainties (blue band). The key feature of our theoretical prediction that matters most in the far-tail region is the merging of the renormalization scales toward $\mu_S = \mu_J = \mu_H$ at $C \sim 0.75$ in the profile functions. This is a necessary condition for the cancellations between singular and non-singular terms in the cross section to occur above the shoulder region.⁴ At $Q = m_Z$ the theoretical cross section

³The OPAL data was excluded from the plot because its bins are rather coarse in this region, making it a bad approximation of the differential cross section.

⁴It is worth mentioning that in the far-tail region we employ the \overline{MS} scheme for Ω_1 , since the subtractions implemented in the Rgap scheme clash with the partonic shoulder singularity, resulting in an unnatural behavior of the cross section around $C = 0.75$. The transition between the Rgap and \overline{MS} schemes is performed smoothly, by means of a hybrid scheme which interpolates between the two in a continuous way. This hybrid scheme has been discussed at length in Ref. [12].

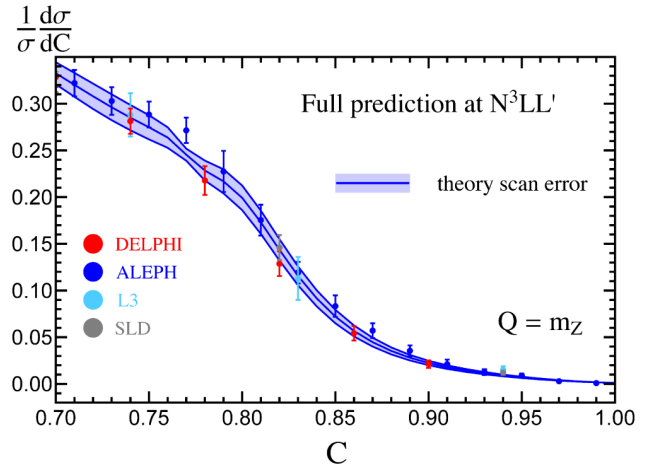


FIG. 12 (color online). C -parameter distribution above the fit range, shown at N^3LL' order for $Q = m_Z$ using the best-fit values for $\alpha_s(m_Z)$ and Ω_1 . Again the blue band corresponds to the theory uncertainty and the error bars are used for experimental data.

presented here obtains accurate predictions in the region both below and above the shoulder that agree with the data. Our analysis does not include the full $\mathcal{O}(\alpha_s^k \Lambda_{QCD}^3/Q)$ power corrections (for $k < 4$), since they are not part of our master formula. Nevertheless, and in analogy with what was found in the case of thrust, agreement with the experimental data seems to indicate that these missing power corrections may be smaller than naively expected.

VII. UNIVERSALITY AND COMPARISON TO THRUST

An additional prediction of our theoretical formalism is the universality of Ω_1 between the thrust and C -parameter event shapes. Therefore, a nontrivial test of our formalism can be made by comparing our result for Ω_1 with the determination from the earlier fits of the thrust tail distributions in Ref. [9] and the first moment of the thrust distribution in Ref. [10].

Since we have updated our profiles for thrust, it is expected that the outcome of the α_s and Ω_1 determination is slightly (within theoretical uncertainties) different from that of Ref. [9]. We also have updated our code to match that of Ref. [10] (higher statistics for the two-loop nonsingular cross sections and using the exact result for the two-loop soft function nonlogarithmic constant). In addition we have corrected the systematic uncertainty for the ALEPH data, $Q = 91.2$ GeV of Ref. [64].⁵ When we compare thrust and C -parameter we neglect bottom-mass and QED effects in

⁵In Ref. [9] we assumed that two quoted uncertainties were asymmetric uncertainties, but it turns out they are two sources of systematic uncertainties that need to be added in quadrature. This has no significant effect on the results of Ref. [9].

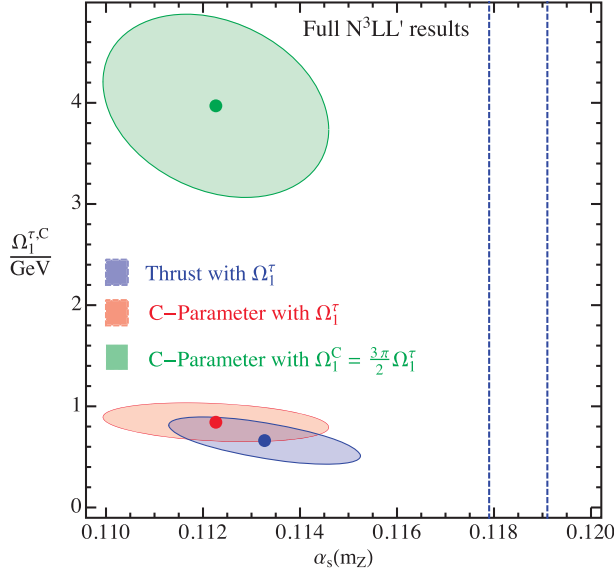


FIG. 13 (color online). Comparison of determinations of $\alpha_s(m_Z)$ and Ω_1 with the corresponding total $1-\sigma$ uncertainty ellipses. As an illustration we display the determination of Ω_1^C obtained from fits to the C-parameter distribution (green), which is clearly different from Ω_1^r obtained from thrust fits (blue), and the determination of Ω_1^r as obtained from C-parameter distribution fits (red). All fits have been performed with N^3LL' theoretical predictions with power corrections and in the Rgap scheme. The dashed vertical lines indicate the PDG 2014 [23] determination of $\alpha_s(m_Z)$.

both event shapes. In this setup, we find an updated result for thrust:

$$\begin{aligned} \alpha_s(m_Z) &= 0.1134 \pm 0.0002_{\text{exp}} \\ &\quad \pm 0.0005_{\text{hadr}} \pm 0.0011_{\text{pert}}, \\ \Omega_1(R_\Delta, \mu_\Delta) &= 0.329 \pm 0.009_{\text{exp}} \\ &\quad \pm 0.021_{\alpha_s(m_Z)} \pm 0.060_{\text{pert}} \text{ GeV}. \end{aligned} \quad (35)$$

For completeness we also quote an updated thrust result when both QED and bottom-mass effects are taken into account:

$$\begin{aligned} \alpha_s(m_Z) &= 0.1128 \pm 0.0002_{\text{exp}} \\ &\quad \pm 0.0005_{\text{hadr}} \pm 0.0011_{\text{pert}}, \\ \Omega_1(R_\Delta, \mu_\Delta) &= 0.322 \pm 0.009_{\text{exp}} \\ &\quad \pm 0.021_{\alpha_s(m_Z)} \pm 0.064_{\text{pert}} \text{ GeV}. \end{aligned} \quad (36)$$

Both the results in Eqs. (35) and (36) are fully compatible at $1-\sigma$ with those in Ref. [9], as discussed in more detail in Appendix C.

When testing for the universality of Ω_1 between thrust and C-parameter, there is an important calculable numerical factor of $3\pi/2 = 4.7$ between Ω_1^r and Ω_1^C that must be accounted for; see Eq. (3). If we instead make a direct

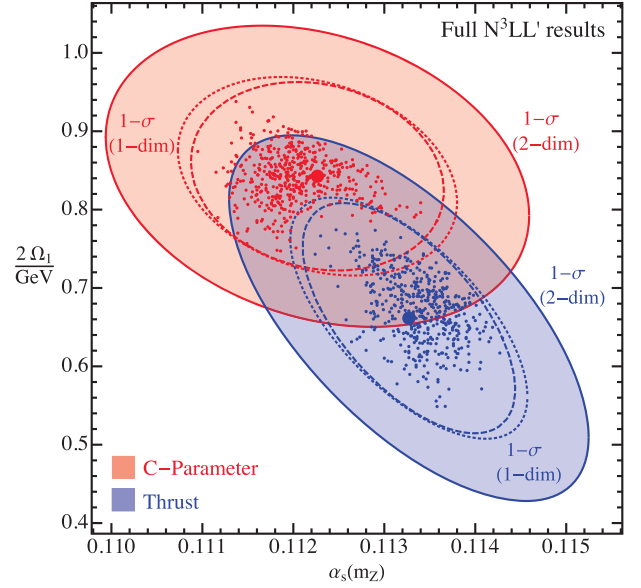


FIG. 14 (color online). Distribution of best-fit points in the $\alpha_s(m_Z)$ - $2\Omega_1$ plane for both thrust (blue) and C-parameter (red) at $N^3LL' + \mathcal{O}(\alpha_s^3) + \Omega_1(R, \mu)$. The outer solid ellipses show the $\Delta\chi^2 = 2.3$ variations, representing $1-\sigma$ uncertainties for two variables. The inner dashed ellipses correspond to the $1-\sigma$ theory uncertainties for each one of the fit parameters. The dotted ellipses correspond to $\Delta\chi^2 = 1$ variations of the total uncertainties. All fits have been performed with N^3LL' theoretical predictions with power corrections and in the Rgap scheme. This plot zooms in on the bottom two ellipses of Fig. 13.

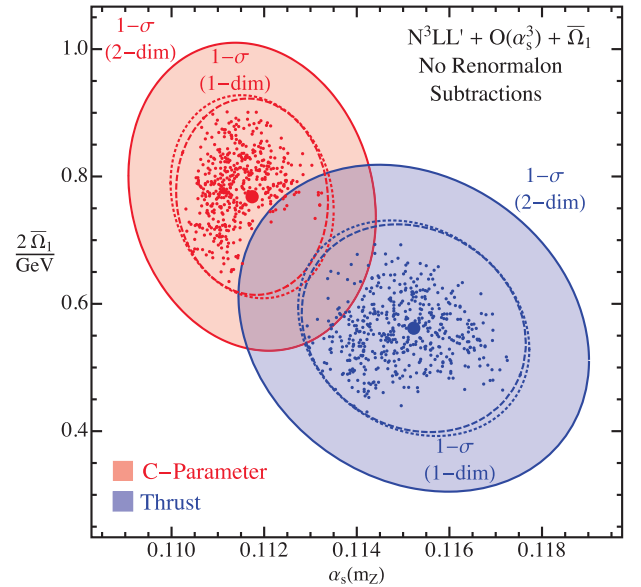


FIG. 15 (color online). Distribution of best-fit points in the $\alpha_s(m_Z)$ - $2\Omega_1$ plane for both thrust (blue) and C-parameter (red) at $N^3LL' + \mathcal{O}(\alpha_s^3) + \overline{\Omega}_1$. The meaning of the different ellipses is the same as in Fig. 14.

comparison of Ω_1^r and Ω_1^C , as shown in Fig. 13 (lowest blue ellipse vs uppermost green ellipse, respectively) then the results are $4.5\text{-}\sigma$ away from each other. Accounting for the $3\pi/2$ factor to convert from Ω_1^C to Ω_1^r the upper green ellipse becomes the centermost red ellipse, and the thrust and C -parameter determinations agree with one another within uncertainties. Due to our high-precision control of perturbative effects, the Ω_1 parameters have only $\sim 15\%$ uncertainty, yielding a test of this universality at a higher level of precision than what has been previously achieved.

A zoomed-in version of this universality plot is shown in Fig. 14. The upper red ellipse again shows the result from fits to the C -parameter distribution, while the lower blue ellipse shows the result from thrust tail fits. For both we show the theory uncertainty (dashed lines) and combined theoretical and experimental (dotted lines) 39% C.L. uncertainty ellipses, as well as the solid ellipses which correspond to $\Delta\chi^2 = 2.3$ which is the standard $1\text{-}\sigma$ uncertainty for a two-parameter fit (68% C.L.). We see that the two analyses are completely compatible at the $1\text{-}\sigma$ level. An important ingredient to improve the overlap is the fact that we define the power corrections in the renormalon-free Rgap scheme. This is shown by contrasting the Rgap result in Fig. 14 with the overlap obtained when using the $\overline{\text{MS}}$ scheme for Ω_1 , as shown in Fig. 15.

VIII. CONCLUSIONS AND COMPARISON TO OTHER α_s DETERMINATIONS

In this paper an accurate determination of α_s from fits to the C -parameter distribution in the resummation region was presented. We fit to the tail of the distribution defined by $3\pi\Lambda_{\text{QCD}}/Q \ll C \lesssim 3/4$, where the dominant hadronization effects are encoded in the first moment of the shape function Ω_1 , which is a power correction to the cross section. By fitting to data at multiple Q 's, the strong coupling $\alpha_s(m_Z)$ and Ω_1 can be simultaneously determined. The key points to our precise theoretical prediction are a) higher-order resummation accuracy ($\text{N}^3\text{LL}'$), achieved through an SCET factorization theorem, b) $\mathcal{O}(\alpha_s^3)$ matrix elements and fixed-order kinematic power corrections, c) field-theoretical treatment of nonperturbative power corrections, and d) switching to a short-distance Rgap scheme, in which the sensitivity to infrared physics is reduced.

As our final result from the C -parameter global fit we obtain

$$\begin{aligned}\alpha_s(m_Z) &= 0.1123 \pm 0.0015, \\ \Omega_1(R_\Delta, \mu_\Delta) &= 0.421 \pm 0.063 \text{ GeV},\end{aligned}\quad (37)$$

where α_s is defined in the $\overline{\text{MS}}$ scheme, and Ω_1 in the Rgap scheme (without hadron-mass effects) at the reference scales $R_\Delta = \mu_\Delta = 2 \text{ GeV}$. Here the respective total $1\text{-}\sigma$ uncertainties are shown. The results with individual $1\text{-}\sigma$

uncertainties quoted separately for the different sources of uncertainties are given in Eq. (34). Neglecting the non-perturbative effects incorporated by Ω_1 , the fit yields $\alpha_s(m_Z) = 0.1219$ which exceeds the result in Eq. (37) by 8%. This is consistent with a simple scaling argument one can derive from experimental data, presented in Ref. [12]. We have also presented an updated thrust result, using our improved profiles for thrust and including bottom-mass and QED effects (but neglecting hadron-mass effects). This *global fit for thrust* gives

$$\begin{aligned}\alpha_s(m_Z) &= 0.1128 \pm 0.0012, \\ \Omega_1(R_\Delta, \mu_\Delta) &= 0.322 \pm 0.068 \text{ GeV}.\end{aligned}\quad (38)$$

Our theoretical prediction is the most complete treatment of C -parameter at this time, and, to the best of our knowledge, all sources of uncertainties have been included in our final uncertainty. Possible improvements which are expected to be negligible relative to our final uncertainty include finite bottom-mass effects, QED effects, and axial-singlet contributions. There are a number of additional theoretical issues that would be interesting to be investigated further in the future. These are common to almost every event-shape analysis in the literature and include (i) resummation of logarithms for the nonsingular partonic cross section; (ii) the structure of nonperturbative power corrections for the nonsingular contributions (the last two points can be clarified with subleading SCET factorization theorems); (iii) analytic perturbative computations of the $\mathcal{O}(\alpha_s^3)$ nonlogarithmic coefficients in the partonic soft function and the jet function, as well as the four-loop QCD cusp anomalous dimension (and to a lesser extent, the numerically determined $s_2^{\tilde{C}}$ constant of the two-loop partonic soft function); (iv) a better understanding of hadron-mass effects, and in particular their resummation beyond NLL; (v) a better theoretical description of the region around and above the shoulder. Concerning (i), and following the common lore, we have incorporated in our analysis the nonsingular contributions in fixed-order perturbation theory. However we have estimated the uncertainty related to the higher-order logarithms through the usual renormalization scale variation. Concerning (ii) we observe that the effect of these neglected power corrections is much smaller than naively expected, as can be seen from a comparison of our theoretical prediction and LEP data in the far-tail region. A first step towards clarifying (i) and (ii) has been taken in Refs. [74,75], for the case of thrust. The computation of missing perturbative terms (iii) is *a priori* feasible with current computational knowledge but they do not dominate our perturbative uncertainties. Concerning (iv) we have shown that hadron-mass effects have a very small impact on the determination of α_s , and hence unless the rest of the sources of uncertainty become substantially smaller, our lack of knowledge does not

constitute a problem. As for (v), our fits do not include data above the shoulder, so this problem has no impact on our fit. Nevertheless an analysis of these subleading effects would be interesting.

The same theoretical program carried out for thrust and C -parameter can be applied to other event shapes, and the most prominent one is heavy jet mass. This has partially worked out already in Ref. [8] at the purely perturbative level using fully canonical profiles. Their determination of α_s is discussed below. For recoil-sensitive observables such as jet broadening [76–80], one needs to deal with rapidity singularities, which imply that additional logs need to be resummed, and more complicated nonperturbative power corrections. The former has been pushed to the N^2LL order in Ref. [81], and the latter has been studied in Ref. [82]. Recoil-insensitive versions of broadening have also been derived [83], but not yet studied experimentally. Finally, it is very straightforward to generalize our theoretical treatment to the case of oriented event shapes [84], in which one additionally measures the angle between the beam and the thrust axes.

At this point we compare our result for α_s with other determinations from event shapes at $\mathcal{O}(\alpha_s^3)$. To the best of our knowledge, the only analyses which fit to the tail of the C -parameter distribution using three-loop input are Ref. [85] (using purely fixed-order perturbation theory) and Ref. [86] (including NLL resummation). Both analyses used Monte Carlo (MC) event generators to estimate hadronization effects, and fit α_s for different Q values, finding values $\alpha_s(m_Z) = 0.1288 \pm 0.0043$ and 0.1252 ± 0.0053 respectively for a fit to the $Q = 91.2$ GeV data. These larger $\alpha_s(m_Z)$ values are consistent with our fits which neglect power corrections, and following Ref. [9] we can conclude from this that Monte Carlo event generators does not provide a reasonable estimate of the power corrections when including the higher-order perturbative contributions. In Ref. [25] two-parameter global fits to the first five moments of the C -parameter distribution were performed. Hadronization effects are included via the frozen coupling model, and the value obtained, $\alpha_s(m_Z) = 0.1181 \pm 0.0048$, is fully consistent with our result in Eq. (37) at $1\text{-}\sigma$.

A graphical comparison with other event-shape determinations is shown in Fig. 16. The figure includes determinations where power corrections are estimated with MC generators, labeled by 7–10. Analyses 1–6 correspond to those in which power corrections were incorporated with an analytic method (either a shape function or the dispersive model). In the analyses 1–6 global fits were performed, whereas in the 7–10 analyses α_s was determined at multiple Q values and the final result is an average of those. Only analyses 1 [10], 3 (this work), and 4 [9] use a completely field-theoretical approach for the power corrections. We also show both results from fits to the event-shape distributions (3–10) and from fits to moments of the event-shape distribution (1 and 2). Although all analyses

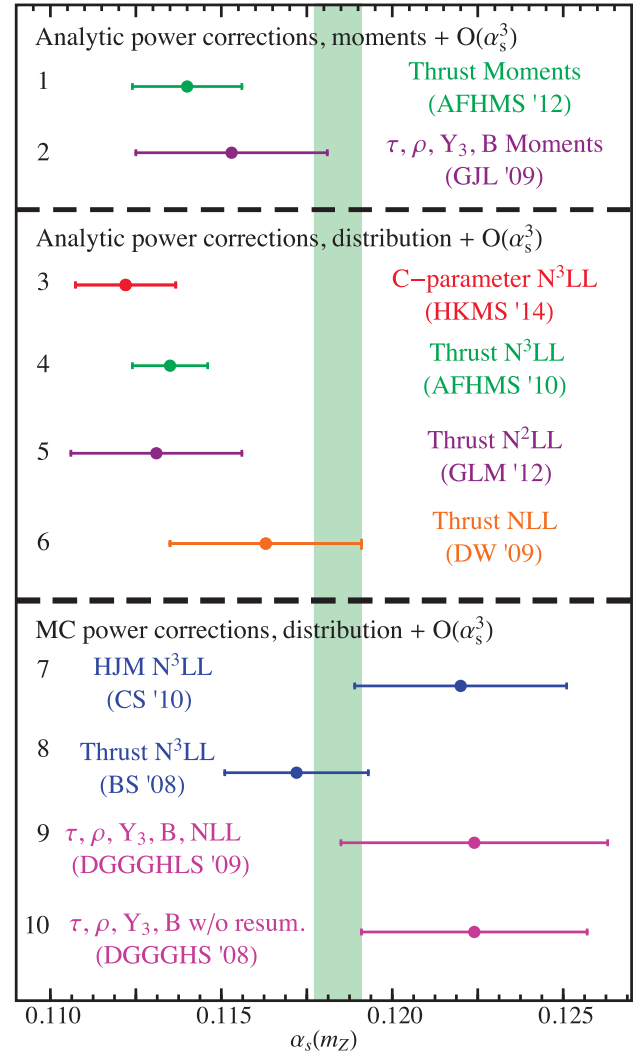


FIG. 16 (color online). Comparison of our determination of $\alpha_s(m_Z)$ (red) with similar analyses from thrust [9,10] (green) and other determinations from fits to event-shape distributions using $\mathcal{O}(\alpha_s^3)$ theory predictions and different levels of resummation. Results shown below the lower dashed line include power corrections as predicted by MC generators, and results above this line treat power corrections either from a shape function (red and green) or from the dispersive model (orange [4] and purple [11]). Determinations above the upper dashed line correspond to fits to moments of the distributions, and those below to fits to the tail of the differential distribution. The translucent green band corresponds to the world average from Ref. [23].

included $\mathcal{O}(\alpha_s^3)$ matrix elements, different levels of resummation have been achieved. Analyses 2 [25] and 10 [85] did not include resummation; 6 [4] and 9 [86] included NLL resummation; 5 [11] included N^2LL resummation; and analyses 3, 4, 7, and 8 included N^3LL resummation. Analyses 2, 9, and 10 simultaneously fit to many event shapes, whereas the others focused on a single observable: thrust (1, 4–6 and 8 [5]), heavy jet mass (7 [8]), and

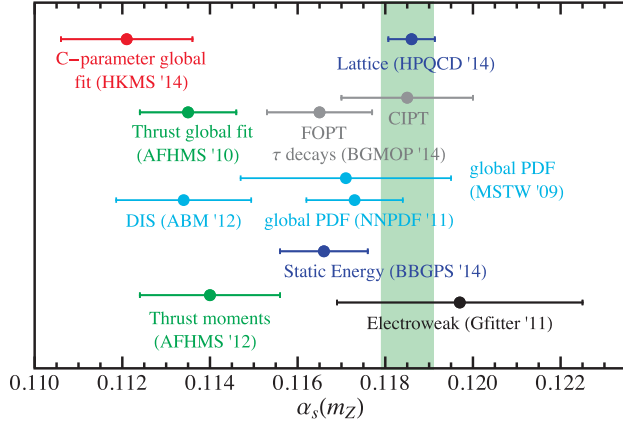


FIG. 17 (color online). Comparison of our determination of $\alpha_s(m_Z)$ (red) with similar previous analyses at N^3LL' for thrust (green) [9,10] and other selected determinations: lattice [24] and static energy potential [29] (both use lattice input, in blue), electroweak precision observables fits [87] (black), deep inelastic scattering [28] and global PDF fits [30,31], and hadron τ decays [27] [fixed-order perturbation theory (FOPT), and contour-improved perturbation theory (CIPT), both in gray]. The current world average [23] is shown as a translucent green band.

C-parameter (3, which is this work). The analyses 1, 3, 4, 7 and 8 used SCET to perform Sudakov log resummation. All results that used an analytic treatment of power corrections have smaller values of α_s . This is consistent with a simple dimensional analysis argument (see Refs. [9,12]). Higher-order resummation results in a convergent perturbation series and smaller uncertainties, and the Rgap scheme also reduces uncertainties. Accounting for the fact that results relying on MC for the treatment of power corrections should likely have larger hadronization uncertainties, all results are compatible among one another. The most precise results are however clearly in disagreement with the world average, which is dominated by lattice QCD results (see below) and shown as a translucent green band.

We conclude this work by comparing our result for $\alpha_s(m_Z)$ with the results of a selection of recent analyses using other techniques and observables, as shown in Fig. 17. We include a next-to-next-to-next-to-leading-order analysis of data from deep inelastic scattering from the ABM group [28], the global PDF fits of the MSTW group [31] and the NNPDF Collaboration [30]; the most recent (and accurate) determination from the HPQCD lattice Collaboration [24], from the analysis of Wilson loops and pseudoscalar correlators; a determination analyzing the lattice prediction for the QCD static potential [29]; a reanalysis of electroweak precision observables by the Gfitter Collaboration [87]; the most recent analysis of tau decays in which the recently released ALEPH data was used together with the OPAL data; the previous determinations from fits to the thrust distribution [9] and moments of the thrust distribution [10]; and of course the

current world average [23] (shown as the green band). The ABM (DIS) and thrust results are compatible with our determination, while in contrast the disagreement with either lattice QCD or the world average is $4\text{-}\sigma$. Many other determinations lie between these two values. The source of this disagreement is an important open question.

ACKNOWLEDGMENTS

We thank the Erwin-Schrödinger Institute (ESI) for partial support in the framework of the ESI program “Jets and Quantum Fields for LHC and Future Colliders.” This work was supported by the offices of Nuclear and Particle Physics of the U.S. Department of Energy (DOE) under Contract DE-SC0011090, and the European Community’s Marie-Curie Research Networks under contract PITN-GA-2010-264564 (LHCphenOnet). I. S. was also supported in part by the Simons Foundation Investigator Grant No 327942. V. M. was supported by a Marie Curie Fellowship under contract PIOF-GA-2009-251174 while part of this work was completed. A. H., V. M., and I. S. are also supported in part by MISTI global seed funds. V. M. thanks H. Stenzel for explaining how to interpret the systematic uncertainties in the ALEPH data set and Thomas Hahn for computer support.

APPENDIX A: PROFILE FORMULAS

In this appendix, we give the details for the profile functions that control the renormalization scales as laid out in Sec. II B. For the soft profile function, we use the form,

$$\mu_S = \begin{cases} \mu_0, & 0 \leq C < t_0, \\ \zeta\left(\mu_0, 0, 0, \frac{r_s \mu_H}{6}, t_0, t_1, C\right), & t_0 \leq C < t_1, \\ r_s \mu_H \frac{C}{6}, & t_1 \leq C < t_2, \\ \zeta\left(0, \frac{r_s \mu_H}{6}, \mu_H, 0, t_2, t_s, C\right), & t_2 \leq C < t_s, \\ \mu_H, & t_s \leq C < 1, \end{cases} \quad (\text{A1})$$

where the physical meaning of the parameters is explained in Sec. II B. The function $\zeta(a_1, b_1, a_2, b_2, t_1, t_2, t)$ (with $t_1 < t_2$), which smoothly connects two straight lines of the form $l_1(t) = a_1 + b_1 t$ for $t < t_1$ and $l_2(t) = a_2 + b_2 t$ for $t > t_2$, is given by

$$\zeta(t) = \begin{cases} \hat{a}_1 + b_1(t - t_1) + e_1(t - t_1)^2, & t_1 \leq t \leq t_m, \\ \hat{a}_2 + b_2(t - t_2) + e_2(t - t_2)^2, & t_m \leq t \leq t_2, \end{cases}$$

$$\hat{a}_1 = a_1 + b_1 t_1, \quad \hat{a}_2 = a_2 + b_2 t_2,$$

$$e_1 = \frac{4(\hat{a}_2 - \hat{a}_1) - (3b_1 + b_2)(t_2 - t_1)}{2(t_2 - t_1)^2},$$

$$e_2 = \frac{4(\hat{a}_1 - \hat{a}_2) + (3b_2 + b_1)(t_2 - t_1)}{2(t_2 - t_1)^2}. \quad (\text{A2})$$

For the jet scale, we use the form

$$\mu_J(C) = \begin{cases} [1 + e_J(C - t_s)^2] \sqrt{\mu_H \mu_S(C)}, & C \leq t_s, \\ \mu_H, & C > t_s, \end{cases} \quad (\text{A3})$$

which allows a slight modification of the natural relation between the scales $\mu_J = \sqrt{\mu_H \mu_S}$ in order to account for theoretical uncertainties.

For the subtraction scale, we have

$$R(C) = \begin{cases} R_0, & 0 \leq C < t_0, \\ \zeta\left(R_0, 0, 0, \frac{r_s \mu_H}{6}, t_0, t_1, C\right), & t_0 \leq C < t_1, \\ \mu_S(C), & t_1 \leq C \leq 1. \end{cases} \quad (\text{A4})$$

As explained earlier, we take $R = \mu_S$ in the resummation region to avoid large logs and $R \neq \mu_S$ in the nonperturbative region to remove the renormalon. The ζ function here interpolates smoothly between these two regions.

It is necessary to vary the profile parameters to estimate the theory uncertainty. We hold the difference between the parameters associated with the purely nonperturbative region constant, $\mu_0 - R_0 = 0.4$ GeV, and we set as default values $\mu_0 = 1.1$ GeV, $R_0 = 0.7$ GeV. We are then left with nine profile parameters to vary during the theory scan, whose central values and variation ranges used in our

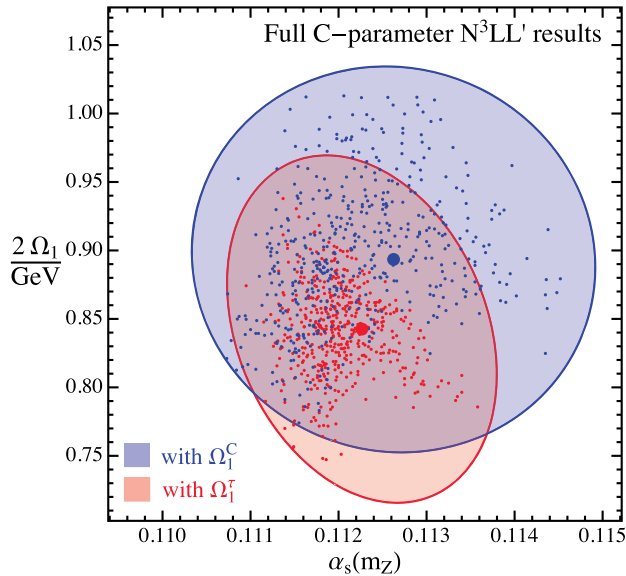


FIG. 18 (color online). Comparison of α_s determinations from C -parameter tail fits in the thrust Rgap scheme (lower red ellipse) and the C -parameter Rgap scheme (upper blue ellipse). The leading power correction Ω_1^C in the C -parameter Rgap scheme is converted to Ω_1 in the thrust Rgap scheme in order to have a meaningful comparison. Theoretical uncertainty ellipses are shown which are suitable for projection onto one dimension to obtain the $1\text{-}\sigma$ uncertainty, without experimental uncertainties.

analysis are: $r_s = 2 \times 1.13^{\pm 1}$, $n_0 = 12 \pm 2$, $n_1 = 25 \pm 3$, $t_2 = 0.67 \pm 0.03$, $t_s = 0.83 \pm 0.03$, $e_J = 0 \pm 0.5$, $e_H = 2^{\pm 1}$ and $n_s = 0 \pm 1$. These variations are shown in Table I.

APPENDIX B: COMPARISON OF THRUST AND C-PARAMETER SUBTRACTIONS

In Fig. 18 we compare fits performed in the Rgap scheme with C -parameter gap subtractions as the upper red ellipse, and for our default fits in the Rgap scheme with thrust gap subtractions as the lower blue ellipse. At N^3LL' order with C -parameter subtractions the results are $\alpha_s(m_Z) = 0.1126 \pm 0.0002_{\text{exp}} \pm 0.0007_{\text{hadr}} \pm 0.0022_{\text{pert}}$ and $\Omega_1(R_\Delta, \mu_\Delta) = 0.447 \pm 0.007_{\text{exp}} \pm 0.018_{\alpha_s} \pm 0.065_{\text{pert}}$ GeV, with $\chi^2_{\text{min}}/\text{d.o.f.} = 0.988$. One can see that, even though both extractions are fully compatible, the thrust subtractions lead to smaller perturbative uncertainties. This is consistent with the better perturbative behavior observed for the cross section with thrust subtractions in Ref. [12].

APPENDIX C: COMPARISON OF THRUST RESULTS WITH REF. [9]

In Fig. 19 we compare global fits for the thrust distribution using the profiles of Ref. [9] (shown by the right ellipse in blue) and the profiles used here (shown by the left ellipse in red). As mentioned earlier, the profiles used here have several advantages over those of Ref. [9] in

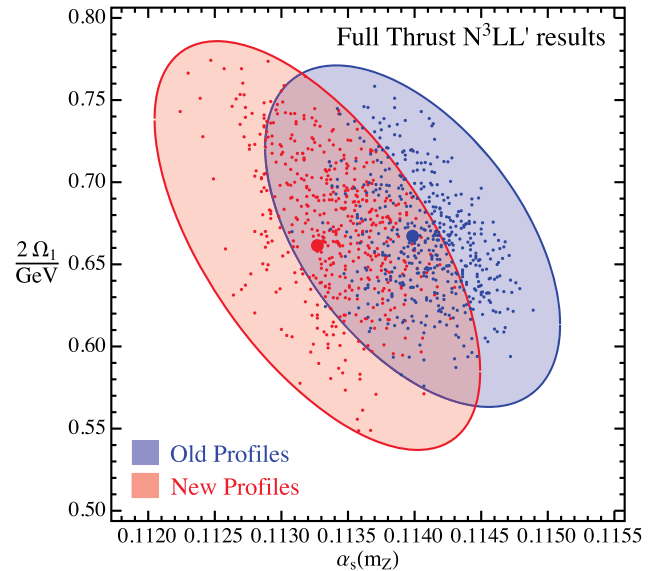


FIG. 19 (color online). Comparison of thrust α_s determinations using our new profiles (left red ellipse) and the profiles of Ref. [9] (right blue ellipse). Theoretical uncertainty ellipses are shown which are suitable for projection onto one dimension to obtain the $1\text{-}\sigma$ uncertainty, without experimental uncertainties.

terms of their ability to independently impact the different regions of the thrust distribution, and in particular do a better job in the nonperturbative region (which is outside our fit region). The two versions of the profiles are

consistent within their variations, and the fit results shown for 39% C.L. for two dimensions in Fig. 19 (which is 68% C.L. for each one-dimensional projection) are fully compatible.

-
- [1] S. Kluth, *Rep. Prog. Phys.* **69**, 1771 (2006).
- [2] S. Bethke *et al.*, *Nucl. Phys. Proc. Suppl.* **234**, 229 (2013).
- [3] A. Gehrmann-De Ridder, T. Gehrmann, E. W. N. Glover, and G. Heinrich, *Phys. Rev. Lett.* **99**, 132002 (2007).
- [4] R. A. Davison and B. R. Webber, *Eur. Phys. J. C* **59**, 13 (2009).
- [5] T. Becher and M. D. Schwartz, *J. High Energy Phys.* **07** (2008) 034.
- [6] G. Dissertori, A. Gehrmann-De Ridder, T. Gehrmann, E. W. N. Glover, G. Heinrich, and H. Stenzel, *Phys. Rev. Lett.* **104**, 072002 (2010).
- [7] A. Gehrmann-De Ridder, T. Gehrmann, E. Glover, and G. Heinrich, *J. High Energy Phys.* **05** (2009) 106.
- [8] Y.-T. Chien and M. D. Schwartz, *J. High Energy Phys.* **08** (2010) 058.
- [9] R. Abbate, M. Fickinger, A. H. Hoang, V. Mateu, and I. W. Stewart, *Phys. Rev. D* **83**, 074021 (2011).
- [10] R. Abbate, M. Fickinger, A. H. Hoang, V. Mateu, and I. W. Stewart, *Phys. Rev. D* **86**, 094002 (2012).
- [11] T. Gehrmann, G. Luisoni, and P. F. Monni, *Eur. Phys. J. C* **73**, 2265 (2013).
- [12] A. H. Hoang, D. W. Kolodrubetz, V. Mateu, and I. W. Stewart, *Phys. Rev. D* **91**, 094017 (2015).
- [13] E. Farhi, *Phys. Rev. Lett.* **39**, 1587 (1977).
- [14] G. Parisi, *Phys. Lett. B* **74**, 65 (1978).
- [15] J. F. Donoghue, F. Low, and S.-Y. Pi, *Phys. Rev. D* **20**, 2759 (1979).
- [16] C. W. Bauer, S. Fleming, and M. E. Luke, *Phys. Rev. D* **63**, 014006 (2001).
- [17] C. W. Bauer, S. Fleming, D. Pirjol, and I. W. Stewart, *Phys. Rev. D* **63**, 114020 (2001).
- [18] C. W. Bauer and I. W. Stewart, *Phys. Lett. B* **516**, 134 (2001).
- [19] C. W. Bauer, D. Pirjol, and I. W. Stewart, *Phys. Rev. D* **65**, 054022 (2002).
- [20] C. W. Bauer, S. Fleming, D. Pirjol, I. Z. Rothstein, and I. W. Stewart, *Phys. Rev. D* **66**, 014017 (2002).
- [21] S. Catani and B. Webber, *J. High Energy Phys.* **10** (1997) 005.
- [22] S. Catani and B. Webber, *Phys. Lett. B* **427**, 377 (1998).
- [23] K. Olive *et al.* (Particle Data Group), *Chin. Phys. C* **38**, 090001 (2014).
- [24] B. Chakraborty, C. T. H. Davies, B. Galloway, P. Knecht, J. Koponen, G. C. Donald, R. J. Dowdall, G. P. Lepage, and C. McNeile, *Phys. Rev. D* **91**, 054508 (2015).
- [25] T. Gehrmann, M. Jaquier, and G. Luisoni, *Eur. Phys. J. C* **67**, 57 (2010).
- [26] A. Banfi, H. McAslan, P. F. Monni, and G. Zanderighi, [arXiv:1412.2126](https://arxiv.org/abs/1412.2126).
- [27] D. Boito, M. Golterman, K. Maltman, J. Osborne, and S. Peris, *Phys. Rev. D* **91**, 034003 (2015).
- [28] S. Alekhin, J. Blumlein, and S. Moch, *Phys. Rev. D* **86**, 054009 (2012).
- [29] A. Bazavov, N. Brambilla, X. Garcia i Tormo, P. Petreczky, J. Soto, and A. Vairo, *Phys. Rev. D* **90**, 074038 (2014).
- [30] R. D. Ball, V. Bertone, L. D. Debbio, S. Forte, A. Guffanti, J. I. Latorre, S. Lionetti, J. Rojo, and M. Ubiali, *Phys. Lett. B* **707**, 66 (2012).
- [31] A. D. Martin, W. J. Stirling, R. S. Thorne, and G. Watt, *Eur. Phys. J. C* **64**, 653 (2009).
- [32] A. Gehrmann-De Ridder, T. Gehrmann, E. W. N. Glover, and G. Heinrich, *J. High Energy Phys.* **12** (2007) 094.
- [33] A. Gehrmann-De Ridder, T. Gehrmann, E. Glover, and G. Heinrich, *Comput. Phys. Commun.* **185**, 3331 (2014).
- [34] S. Weinzierl, *Phys. Rev. Lett.* **101**, 162001 (2008).
- [35] S. Weinzierl, *J. High Energy Phys.* **06** (2009) 041.
- [36] A. H. Hoang and I. W. Stewart, *Phys. Lett. B* **660**, 483 (2008).
- [37] Z. Ligeti, I. W. Stewart, and F. J. Tackmann, *Phys. Rev. D* **78**, 114014 (2008).
- [38] E. Gardi and L. Magnea, *J. High Energy Phys.* **08** (2003) 030.
- [39] G. P. Korchemsky and S. Tafat, *J. High Energy Phys.* **10** (2000) 010.
- [40] Y. L. Dokshitzer and B. R. Webber, *Phys. Lett. B* **352**, 451 (1995).
- [41] C. Lee and G. Sterman, *Phys. Rev. D* **75**, 014022 (2007).
- [42] G. P. Salam and D. Wicke, *J. High Energy Phys.* **05** (2001) 061.
- [43] V. Mateu, I. W. Stewart, and J. Thaler, *Phys. Rev. D* **87**, 014025 (2013).
- [44] E. Lunghi, D. Pirjol, and D. Wyler, *Nucl. Phys.* **B649**, 349 (2003).
- [45] C. W. Bauer and A. V. Manohar, *Phys. Rev. D* **70**, 034024 (2004).
- [46] T. Becher and M. Neubert, *Phys. Lett. B* **637**, 251 (2006).
- [47] S. Moch, J. A. M. Vermaseren, and A. Vogt, *Nucl. Phys.* **B688**, 101 (2004).
- [48] T. Matsuura and W. L. van Neerven, *Z. Phys. C* **38**, 623 (1988).
- [49] T. Matsuura, S. C. van der Marck, and W. L. van Neerven, *Nucl. Phys.* **B319**, 570 (1989).
- [50] T. Gehrmann, T. Huber, and D. Maitre, *Phys. Lett. B* **622**, 295 (2005).
- [51] S. Moch, J. A. M. Vermaseren, and A. Vogt, *J. High Energy Phys.* **08** (2005) 049.
- [52] R. N. Lee, A. V. Smirnov, and V. A. Smirnov, *J. High Energy Phys.* **04** (2010) 020.

- [53] P. A. Baikov, K. G. Chetyrkin, A. V. Smirnov, V. A. Smirnov, and M. Steinhauser, *Phys. Rev. Lett.* **102**, 212002 (2009).
- [54] T. Gehrmann, E. Glover, T. Huber, N. Ikizlerli, and C. Studerus, *J. High Energy Phys.* **06** (2010) 094.
- [55] W. L. van Neerven, *Nucl. Phys.* **B268**, 453 (1986).
- [56] R. K. Ellis, D. Ross, and A. Terrano, *Phys. Rev. Lett.* **45**, 1226 (1980).
- [57] R. K. Ellis, D. A. Ross, and A. E. Terrano, *Nucl. Phys.* **B178**, 421 (1981).
- [58] S. Catani and M. H. Seymour, *Phys. Lett. B* **378**, 287 (1996).
- [59] S. Catani and M. H. Seymour, *Nucl. Phys.* **B485**, 291 (1997).
- [60] A. H. Hoang and S. Kluth, [arXiv:0806.3852](https://arxiv.org/abs/0806.3852).
- [61] A. H. Hoang, A. Jain, I. Scimemi, and I. W. Stewart, *Phys. Rev. D* **82**, 011501 (2010).
- [62] Mathematica 10, <http://www.wolfram.com/mathematica/>.
- [63] GFortran, <https://gcc.gnu.org/fortran/>.
- [64] A. Heister *et al.* (ALEPH), *Eur. Phys. J. C* **35**, 457 (2004).
- [65] J. Abdallah *et al.* (DELPHI Collaboration), *Eur. Phys. J. C* **37**, 1 (2004).
- [66] P. Abreu *et al.* (DELPHI), *Z. Phys. C* **73**, 229 (1997).
- [67] P. Abreu *et al.* (DELPHI), *Phys. Lett. B* **456**, 322 (1999).
- [68] D. Wicke, PhD thesis, BUGH Wuppertal, wU-B-DIS-1999-05 (1999).
- [69] O. Biebel, P. M. Fernandez, and S. Bethke (JADE Collaboration), *Phys. Lett. B* **459**, 326 (1999).
- [70] P. Achard *et al.* (L3 Collaboration), *Phys. Rep.* **399**, 71 (2004).
- [71] B. Adeva *et al.* (L3 Collaboration), *Z. Phys. C* **55**, 39 (1992).
- [72] G. Abbiendi *et al.* (OPAL Collaboration), *Eur. Phys. J. C* **40**, 287 (2005).
- [73] K. Abe *et al.* (SLD Collaboration), *Phys. Rev. D* **51**, 962 (1995).
- [74] S. M. Freedman, [arXiv:1303.1558](https://arxiv.org/abs/1303.1558).
- [75] S. M. Freedman and R. Goerke, *Phys. Rev. D* **90**, 114010 (2014).
- [76] S. Catani, G. Turnock, and B. Webber, *Phys. Lett. B* **295**, 269 (1992).
- [77] Y. L. Dokshitzer, A. Lucenti, G. Marchesini, and G. Salam, *J. High Energy Phys.* **01** (1998) 011.
- [78] J.-y. Chiu, A. Jain, D. Neill, and I. Z. Rothstein, *Phys. Rev. Lett.* **108**, 151601 (2012).
- [79] T. Becher, G. Bell, and M. Neubert, *Phys. Lett. B* **704**, 276 (2011).
- [80] J.-Y. Chiu, A. Jain, D. Neill, and I. Z. Rothstein, *J. High Energy Phys.* **05** (2012) 084.
- [81] T. Becher and G. Bell, *J. High Energy Phys.* **11** (2012) 126.
- [82] T. Becher and G. Bell, *Phys. Rev. Lett.* **112**, 182002 (2014).
- [83] A. J. Larkoski, D. Neill, and J. Thaler, *J. High Energy Phys.* **04** (2014) 017.
- [84] V. Mateu and G. Rodrigo, *J. High Energy Phys.* **11** (2013) 030.
- [85] G. Dissertori, A. Gehrmann-De Ridder, T. Gehrmann, E. W. N. Glover, G. Heinrich, and H. Stenzel, *J. High Energy Phys.* **02** (2008) 040.
- [86] G. Dissertori, G. Dissertori, A. Gehrmann-De Ridder, T. Gehrmann, E. W. N. Glover, G. Heinrich, G. Luisoni, and H. Stenzel, *J. High Energy Phys.* **08** (2009) 036.
- [87] H. Flacher, M. Goebel, J. Haller, A. Hoecker, K. Mönig, and J. Stelzer, *Eur. Phys. J. C* **60**, 543 (2009).